

Theoretical modeling of triboelectric nanogenerators (TENGs) F

Cite as: J. Appl. Phys. **128**, 111101 (2020); <https://doi.org/10.1063/5.0020961>

Submitted: 07 July 2020 . Accepted: 23 August 2020 . Published Online: 17 September 2020

Jiajia Shao , Morten Willatzen , and Zhong Lin Wang 

COLLECTIONS

F This paper was selected as Featured



View Online



Export Citation



CrossMark

Lock-in Amplifiers
up to 600 MHz



Theoretical modeling of triboelectric nanogenerators (TENGs)

Cite as: J. Appl. Phys. **128**, 111101 (2020); doi: [10.1063/5.0020961](https://doi.org/10.1063/5.0020961)

Submitted: 7 July 2020 · Accepted: 23 August 2020 ·

Published Online: 17 September 2020



View Online



Export Citation



CrossMark

Jiajia Shao,^{1,2}  Morten Willatzen,^{1,2,a)}  and Zhong Lin Wang^{1,2,3,a)} 

AFFILIATIONS

¹CAS Center for Excellence in Nanoscience, Beijing Key Laboratory of Micro-nano Energy and Sensor, Beijing Institute of Nanoenergy and Nanosystems, Chinese Academy of Sciences, Beijing 100083, China

²College of Nanoscience and Technology, University of Chinese Academy of Sciences, Beijing 100049, People's Republic of China

³School of Materials Science and Engineering, Georgia Institute of Technology, Atlanta, Georgia 30332-0245, USA

^{a)}Authors to whom correspondence should be addressed: mortenwillatzen@binn.cas.cn and zhong.wang@mse.gatech.edu

ABSTRACT

Triboelectric nanogenerators (TENGs), using Maxwell's displacement current as the driving force, can effectively convert mechanical energy into electricity. In this work, an extensive review of theoretical models of TENGs is presented. Based on Maxwell's equations, a formal physical model is established referred to as the quasi-electrostatic model of a TENG. Since a TENG is electrically neutral at any time owing to the low operation frequency, it is conveniently regarded as a lumped circuit element. Then, using the lumped parameter equivalent circuit theory, the conventional capacitive model and Norton's equivalent circuit model are derived. Optimal conditions for power, voltage, and total energy conversion efficiency can be calculated. The presented TENG models provide an effective theoretical foundation for understanding and predicting the performance of TENGs for practical applications.

Published under license by AIP Publishing. <https://doi.org/10.1063/5.0020961>

I. INTRODUCTION

Triboelectric nanogenerators (TENGs) use Maxwell's displacement current as the driving force to convert mechanical energy into electricity, which is a cutting-edge technology in the field of energy harvesting at the small scale.^{1–5} Based on the effects of contact electrification (CE) and electrostatic induction, TENGs essentially belong to the family of mechanical energy harvesters.^{6–8} As of now, four main effects have been utilized to convert mechanical energy into electric energy: electromagnetic induction, piezoelectric, electrostatic, and triboelectric effects.^{9–12} The electromagnetic device is based on electromagnetic induction according to Lenz's law, while the other three devices are governed by Maxwell's displacement current (Fig. 1). Among these techniques, TENGs are probably the most effective approach for energy conversion.^{13–17}

In this review, we present various theoretical models for describing TENGs:

- (a) formal physical models of TENGs;
- (b) equivalent electrical circuit models of TENGs;

- (c) electromechanical coupling model of a TENG in an energy harvesting system; and
- (d) relationship among various models.

II. MECHANISMS FOR ENERGY HARVESTING

Mechanical energy is converted into electric power using four effects: electromagnetic induction, piezoelectric, electrostatic, and triboelectric effects.^{8,9,11} Each harvesting principle has its own characteristics. Electromagnetic harvesters are more common for larger-size devices, while piezoelectric and electrostatic devices are suitable for small scale energy harvesters.^{18,19} The basic structure of an electrostatic harvester is similar to that of the TENG device but the ways of generating and transporting electric charges are different. In a TENG, tribocharges are created because of CE; whereas an external supply source is required to polarize the capacitor material of an electrostatic harvester, and electret materials are utilized to convert mechanical power into electricity.^{20–23} Except for the electromagnetic device, the three other types of harvesters are based on generation of Maxwell's displacement current as a consequence of a

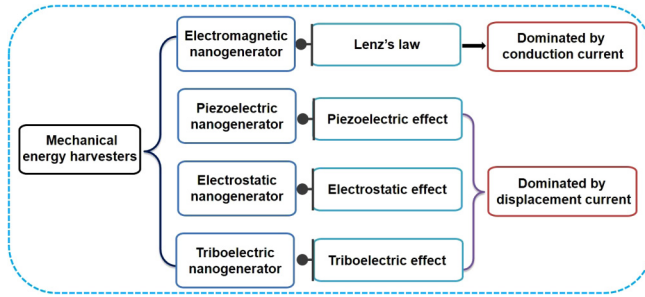


FIG. 1. Four main mechanical energy harvesters based on Lenz's law, the piezoelectric effect, the electrostatic effect, and the triboelectric effect. The electromagnetic nanogenerator is described by the conduction current while other three nanogenerator types are described by displacement current.

time-varying electric field and polarization in the dielectric material.^{1,2} Further details are provided in this review.

The TENG device is one of several types of electromechanical transducers in modern energy harvesting systems associated with a large number of applications in self-powered sensors, blue energy, robotics, environmental protection, wearable electronics, and so on.²⁴⁻³⁹ However, energy conversion and transportation in a TENG energy harvesting system is not fully presented due to the complexity of the physical mechanisms involved; in particular related to CE. Consider a TENG harvester as shown schematically in Fig. 2. The TENG device is composed of two electrodes and two different dielectric materials. One electrode is fixed (right), while the other moves under the action of an external mechanical force. When CE occurs between the two dielectric materials, tribocharges are produced on the contacting surfaces. As a result, the dielectric materials are polarized due to the generation of an electric field originating from the generated charge distributions. In this way, mechanical energy is converted and stored in a TENG device. Note that due to the TENG's constant and relatively slow movement, the stored energy can be treated in a quasi-electrostatic manner, which is

essentially its electrical energy. It is different with the descriptions in Ref. 27. As the relative displacement of the moving electrode changes, the quasi-electrostatic energy changes. Thus, an intermediate system is needed to transfer the generated electrical energy.

As illustrated in Fig. 2, we arrange a connection of a TENG transducer to a vibrating environment. The movable part of a TENG is suspended on a spring (k) and serves as a proof mass (which is a known quantity of mass and utilized as a reference in the measuring instrument). The spring is attached to an external frame placed in the environment, from which mechanical energy is harvested. In a realistic mechanical system a certain part of the energy is always lost due to dissipation (such as air damping), hence a damper model is added here. In essence, this is a mass-spring-damper system (a damped resonator). The movable electrode (proof mass) is part of the resonator and the TENG transducer. Therefore, the TENG device couples the mechanical energy and electrical energy fields. And the electrical energy is controlled by the power management circuit. Note that the inverted arrow indicates that the TENG transducer produces interaction effects between the external mechanical trigger and the conditioning circuit. This process is regarded as the reverse coupling effect.

III. FORMAL PHYSICAL MODELS OF TENGs

A. The first-principle theory of TENGs

Several types of models for the TENG device have been developed (Fig. 3). The first category is the formal physical model such as the quasi-electrostatic models, which is based on the classical electromagnetic theory.⁴⁰⁻⁴⁸ It is important to note that the methods of three-dimensional (3D) mathematical modeling and distance-dependent electric field (DDEF) modeling are established according to the quasi-electrostatic model.^{4,46-48} The second category is an equivalent electrical circuit model that basically contains the CA model and Norton's equivalent circuit model based on the lumped parameter circuit theory.^{40,41,43} As demonstrated in Fig. 3, the formal physical model and the equivalent electrical circuit model are linked to each other and described by a transport

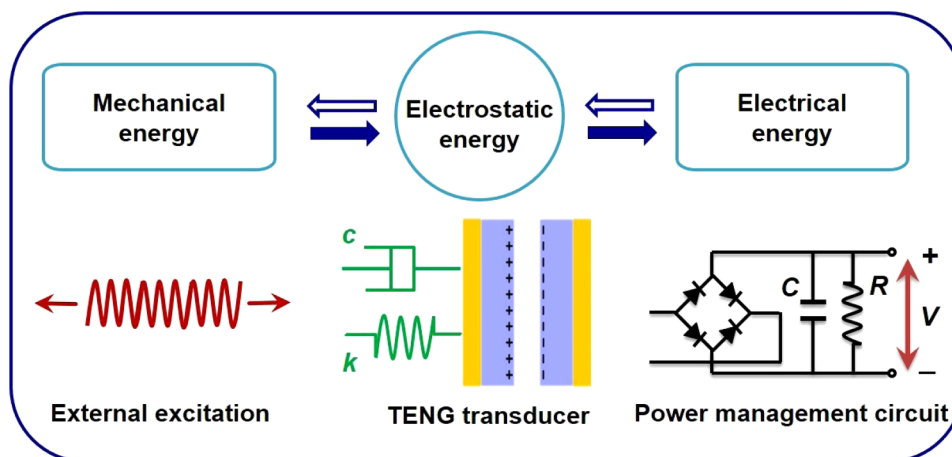


FIG. 2. General energy flow in a mechanical energy harvesting system including an external excitation, a TENG transducer, and a power management circuit. Mechanical energy is transferred and stored in the TENG transducer in the form of electrostatic energy, and then extracted to the external circuit. The bi-directional arrows indicate that each component of the harvesting system affects the upstream components. The TENG transducer couples the mechanical energy and electrical energy.

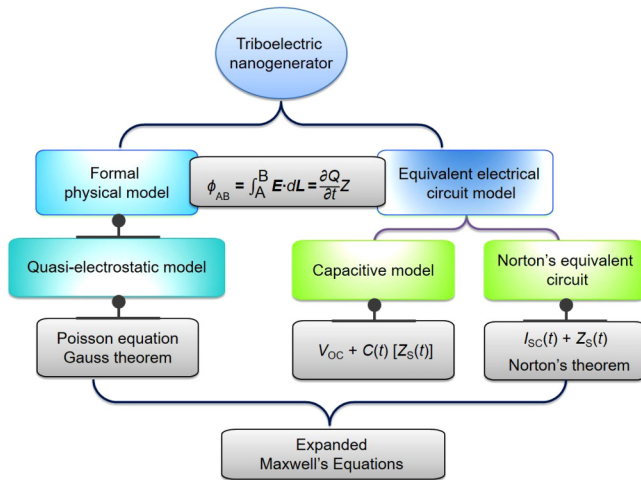


FIG. 3. Models of TENGs including the formal physical model and equivalent electrical circuit model as well as the relationships between them. Note that the formal physical model and equivalent electrical circuit model are linked to each other by a transport equation.

equation. The left-hand side of this equation is the potential drop (ϕ_{AB}) of the TENG device, while the right-hand side is the voltage ($V = \partial Q / \partial t \times Z$) across the external load. According to Kirchhoff's voltage law, the potential difference between the two electrodes of TENG is equal to the voltage across the load resistance, thus the transport equation is obtained. The physics of TENGs is determined

by the variation of potential (ϕ), electric field (E), polarization of the dielectric material (P), and Maxwell's displacement current (I_D). The circuit models determine the outputs from the external circuit such as the variation of voltage (V), current (I), power (P), and extracted electrical energy (E). All these models are described by the expanded Maxwell's equations proposed by Wang.²

As shown in Fig. 4, Maxwell's equations are expanded primarily through the addition term P_S (Fig. 4), known as the Wang term.^{1,2,44} The Wang term originates from the presence of electrostatic surface charges and is, therefore, not a result of the electric-field induced medium polarization P . Hence, adding the Wang term to D ,

$$D = \epsilon_0 E + P + P_S, \tag{1}$$

the corresponding displacement current density J_D is given by

$$J_D = \frac{\partial D}{\partial t} = \epsilon_0 \frac{\partial E}{\partial t} + \frac{\partial P}{\partial t} + \frac{\partial P_S}{\partial t} = \epsilon \frac{\partial E}{\partial t} + \frac{\partial P_S}{\partial t}, \tag{2}$$

where ϵ_0 represents the permittivity of free space (vacuum); ϵ is called the permittivity of the material (or medium), and $\epsilon \equiv \epsilon_0(1 + \chi_e)$, where χ_e represents the electric susceptibility of the medium. Then, we have $P = (\epsilon - \epsilon_0)E$, which accounts for only the polarization in the medium owing to the presence of electric field, as in the standard text book. However, with considering the presence of electrostatic charges on surfaces owing to the piezoelectric or triboelectric effect, the new term P_S must be added in Maxwell's electric displacement to represent the non-electric field induced polarization due to mechanical triggering (contact electrification).

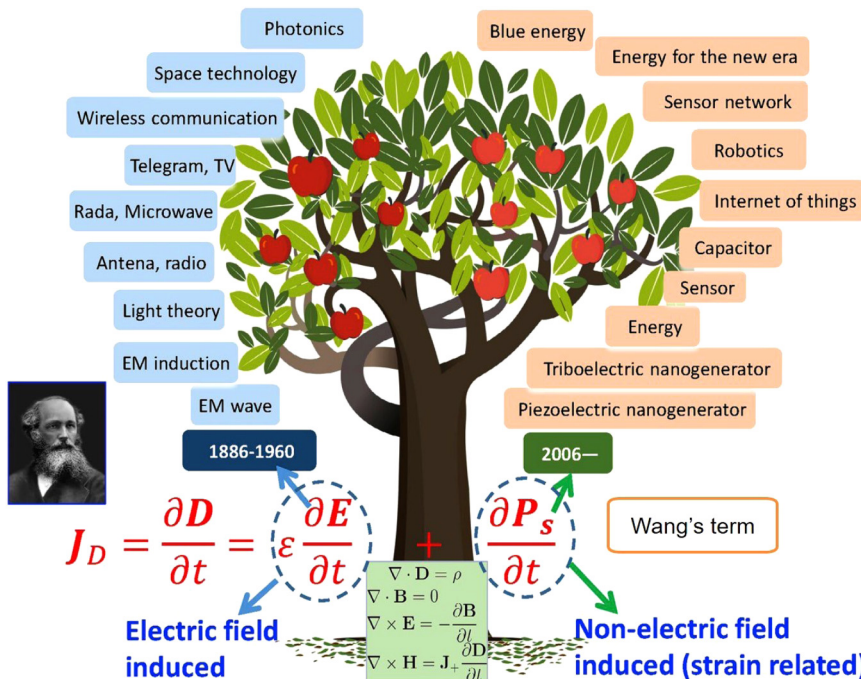


FIG. 4. A comparison of displacement current between Maxwell's equation and Wang's expanded equation. The first term $\epsilon \partial E / \partial t$ in J_D induced by electric field is given by Maxwell in 1861; while the second term $\epsilon \partial P_S / \partial t$ was firstly proposed by Wang in 2017. The displacement current density J_D is the governing principle behind mechanical energy harvesters based on piezoelectricity, electrostatics, and triboelectricity.² Reproduced with permission from Wang, Nano Energy 68, 104272 (2020). Copyright 2020 Elsevier.

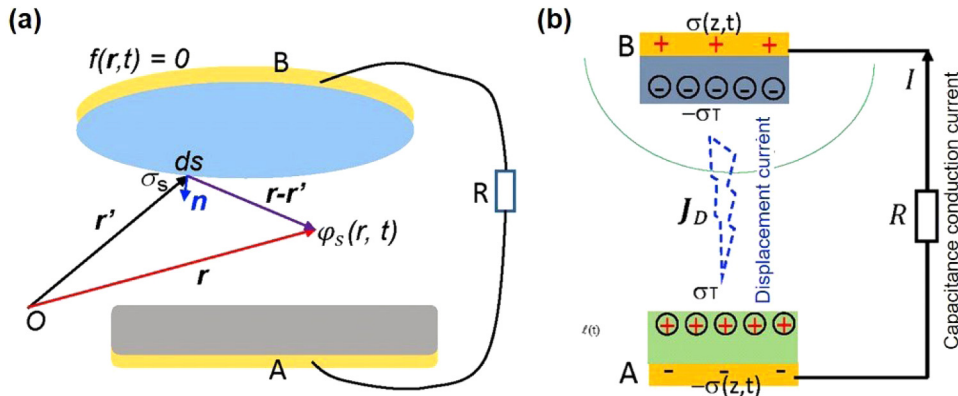


FIG. 5. (a) Schematic illustration of a nanogenerator which can be abstracted as a lumped element with potential difference given by $\phi_{AB} = \int_A^B \mathbf{E} \cdot d\mathbf{L} = \frac{\partial Q}{\partial t} R$; (b) a typical vertical contact-separation mode TENG described by the displacement current within the TENG and conduction current in the external circuit.² Reproduced with permission from Wang, Nano Energy **68**, 104272 (2020). Copyright 2020 Elsevier.

Thus, there is a distinct difference in the physical origin between \mathbf{P} and \mathbf{P}_s . In addition, the volume charge density and the density of current density are redefined by

$$\rho' = \rho - \nabla \cdot \mathbf{P}_s, \tag{3}$$

$$\mathbf{J}' = \mathbf{J} + \frac{\partial \mathbf{P}_s}{\partial t}, \tag{4}$$

satisfying the charge conversion and continuation equation:

$$\nabla \cdot \mathbf{J}' + \frac{\partial \rho'}{\partial t} = 0. \tag{5}$$

As the result, Maxwell's equations are rewritten as

$$\nabla \cdot \mathbf{D}' = \rho', \tag{6.a}$$

$$\nabla \cdot \mathbf{B} = 0, \tag{6.b}$$

$$\nabla \times \mathbf{E} = -\frac{\partial \mathbf{B}}{\partial t}, \tag{6.c}$$

$$\nabla \times \mathbf{H} = \mathbf{J}' + \frac{\partial \mathbf{D}'}{\partial t}. \tag{6.d}$$

The above four self-consistent equations describe the relations among electromagnetic fields and charges as well as current distributions in TENGs. The term $(\epsilon \partial \mathbf{E} / \partial t)$ in Eq. (2) is the well-known contribution to Maxwell's displacement current. The last term $(\partial \mathbf{P}_s / \partial t)$ in Eq. (2) represents the displacement current due to the presence of surface charges that does not depend on the electric field. Further, while the first term is important at high frequencies, the second term provides an important energy generation contribution at low frequencies.^{2,4,6}

For the potential difference between the two electrodes, it can be calculated by (Fig. 5)²

$$\phi_{AB} = \int_A^B \mathbf{E} \cdot d\mathbf{L} = \frac{\partial Q}{\partial t} Z. \tag{7}$$

Note that this equation represents a link between the internal circuit and external circuit of TENG device. On the other hand, the displacement current I_D , calculated by a surface integral of \mathbf{J}_D , is^{2,3,44}

$$I_D = \int \mathbf{J}_D \cdot d\mathbf{s} = \int \frac{\partial \mathbf{D}}{\partial t} \cdot d\mathbf{s} = \frac{\partial}{\partial t} \int (\nabla \cdot \mathbf{D}) dr = \frac{\partial}{\partial t} \int \rho dr = \frac{\partial Q}{\partial t}. \tag{8}$$

Here, Q is the free charge on the electrode. Several conclusions are obtained:²

- (a) The driving force internally in TENGs is the displacement current, while the current received on the load is the conduction current.
- (b) The displacement current is equal to the conduction current at the electrodes under ideal conditions (no losses/leakage currents).
- (c) The displacement and conduction currents join at the electrodes of TENGs forming a complete loop. For piezoelectric, electrostatic, and electret effects-based generators, the generation of current is driven by the displacement current inside the nanogenerators. From the generalized Maxwell's equations, we have obtained the driving force and governing equation of TENG device. The TENG's output characteristics can be predicted completely through formal physical and equivalent electrical circuit models which are discussed as following.

B. Quasi-electrostatic model of TENGs

1. General theory of the electric potential

First, suppose the medium is composed of different dielectric materials containing tribocharges. The composed medium is sandwiched between two electrodes containing free charges [Fig. 6(c)].

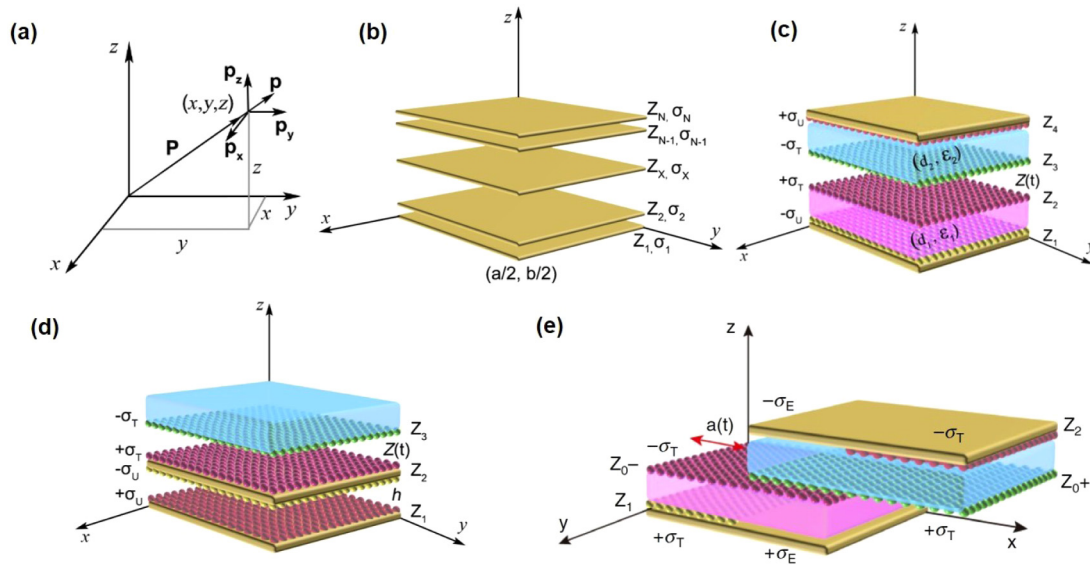


FIG. 6. (a) Schematic illustration of a conventional Cartesian coordinate system; (b) a set of finite-sized charged planes with the charge density $\sigma_1, \sigma_2, \dots, \sigma_N$ at the position of z_1, z_2, \dots, z_N , which are all centered at the position of $(0, 0)$ and constructed in the Cartesian coordinate system; (c)–(e) sketches of the vertical contact-separation mode TENG, single electrode contact mode TENG and lateral-sliding mode TENG in the Cartesian coordinate system with different charge densities on the planes. Reproduced with permission from Shao *et al.*, *Nano Energy* **60**, 630 (2019). Copyright 2019 Elsevier.

The Maxwell–Poisson equation is⁴

$$\nabla \cdot \mathbf{D} = \rho(\mathbf{r}), \tag{9}$$

where ρ is the charge density composed of free charges on the surface of the electrodes and tribocharges in the media. Solving this equation, an integral solution for the electric potential (ϕ) in the dielectric material α is

$$\phi(\mathbf{r}) = \frac{1}{4\pi\epsilon_\alpha} \int \frac{\rho(\mathbf{r}')}{|\mathbf{r} - \mathbf{r}'|} dV, \tag{10}$$

where ϵ_α represents the constant permittivity of the dielectric media α . This is a starting point for the method of 3D mathematical modeling for TENGs.

A Cartesian coordinate system is schematically illustrated in Fig. 6(a) represented by unit vectors \mathbf{e}_x , \mathbf{e}_y , and \mathbf{e}_z . Suppose we have N finite-sized planes, all with the same geometric dimensions a and b along the x and y directions, respectively. These planes are all centered at $(x, y) = (0, 0)$ and located at positions z_1, \dots, z_N with

surface charge densities $\sigma_1, \dots, \sigma_N$, respectively [Fig. 6(b)]. According to Eq. (10), the electrical potential at an arbitrary point $\mathbf{r} = (x, y, z)$ is⁴

$$\begin{aligned} \phi(x, y, z) &= \sum_{i=1}^N \int_{-a/2}^{a/2} \int_{-b/2}^{b/2} \frac{\sigma_i dx' dy'}{4\pi\epsilon(\mathbf{r}) \sqrt{(x-x')^2 + (y-y')^2 + (z-z'_i)^2}} \\ &= \sum_{i=1}^N \frac{\sigma_i}{4\pi\epsilon(\mathbf{r})} \int_{-a/2}^{a/2} \int_{-b/2}^{b/2} \frac{dx' dy'}{\sqrt{(x-x')^2 + (y-y')^2 + (z-z'_i)^2}}. \end{aligned} \tag{11}$$

This equation will be used to calculate the electric potential in the 3D mathematical model.

2. General theory of the electric field and displacement current

From Eq. (11), the relevant electric field is⁴

$$\begin{aligned} \mathbf{E}(x, y, z) &= -\nabla \phi \\ &= \sum_{i=1}^N \frac{\sigma_i}{4\pi\epsilon(\mathbf{r})} \int_{-a/2}^{a/2} \int_{-b/2}^{b/2} \frac{dx' dy'}{\sqrt{(x-x')^2 + (y-y')^2 + (z-z'_i)^2}} \frac{(x-x', y-y', z-z'_i)}{\sqrt{(x-x')^2 + (y-y')^2 + (z-z'_i)^2}}, \end{aligned} \tag{12}$$

where $\epsilon_\alpha = \epsilon(\mathbf{r})$. From symmetry considerations, E_x and E_y vanish identically upon integration over x' and y' . Therefore, the electric field component along the z direction is

$$E_z(0, 0, z) = \sum_{i=1}^N \frac{\sigma_i(z - z'_i)}{4\pi\epsilon(\mathbf{r})} \int_{-a/2}^{a/2} \int_{-b/2}^{b/2} \frac{dx' dy'}{[x'^2 + y'^2 + (z - z'_i)^2]^{3/2}}. \tag{13}$$

If these charged N -finite-sized planes are fixed at positions z_1, \dots, z_N , respectively, the electric field originating from these charge distributions will not change, which leads to generation of an electrostatic field for the three-dimensional space frame.

However, when part of the charged planes move with a very low frequency, a change of total electric field occurs. In other words, the electrostatic model will change to a quasi-electrostatic model for this 3D structure. Based on this quasi-electrostatic model, the methods of 3D mathematical modeling and DDEF modeling have been proposed to investigate the physical variables of the TENG device.^{4,46-48}

Consider the CS model TENG as an example [Fig. 6(c)]. When a load resistance is connected between the two electrodes, charges will be transferred from one electrode to the other to reduce the potential difference. Thus, the presence of four charged plans in the CS mode TENG device allows us to write for the electric field at position z ,

$$E_z(0, 0, z) = -\frac{\sigma_U}{\pi\epsilon(z)} \arctan\left(\frac{ab}{4(z - z_1)\sqrt{\left(\frac{a}{2}\right)^2 + \left(\frac{b}{2}\right)^2 + (z - z_1)^2}}\right) + \frac{\sigma_T}{\pi\epsilon(z)} \arctan\left(\frac{ab}{4(z - z_2)\sqrt{\left(\frac{a}{2}\right)^2 + \left(\frac{b}{2}\right)^2 + (z - z_2)^2}}\right) - \frac{\sigma_T}{\pi\epsilon(z)} \arctan\left(\frac{ab}{4(z - z_3)\sqrt{\left(\frac{a}{2}\right)^2 + \left(\frac{b}{2}\right)^2 + (z - z_3)^2}}\right) + \frac{\sigma_U}{\pi\epsilon(z)} \arctan\left(\frac{ab}{4(z - z_4)\sqrt{\left(\frac{a}{2}\right)^2 + \left(\frac{b}{2}\right)^2 + (z - z_4)^2}}\right), \tag{14}$$

where σ_T and σ_U represent the tribocharge density and transferred charge density between the two electrodes, respectively, and $\epsilon(z)$ is the permittivity at position z . Note that $\epsilon(z)$ is a step function. Using this equation, the electric field inside the air gap [$E_{z,\text{air}}(0, 0, z_{\text{air}})$], dielectric 1 [$E_{z,\text{d1}}(0, 0, z_{\text{d1}})$], and dielectric 2 [$E_{z,\text{d2}}(0, 0, z_{\text{d2}})$] can be calculated, respectively.

According to the definition of the displacement current, the displacement current through a surface S is given by⁴

$$I_D = \int_S \frac{\partial \mathbf{D}}{\partial t} \cdot \mathbf{n} dS, \tag{15}$$

where \mathbf{n} is a normal vector to the surface element dS . Based on Eq. (13), the displacement current along the z direction is

$$I_D = \sum_{i=1}^N \int_S dS \frac{\partial}{\partial t} \left(\frac{\sigma_i}{4\pi} \int_{-a/2}^{a/2} \int_{-b/2}^{b/2} dx' dy' \frac{z - z_i}{[(x - x')^2 + (y - y')^2 + (z - z'_i)^2]^{3/2}} \right), \tag{16}$$

when the S integration extends over the full x - y plane. Including in the integration the region outside the area defined by the plates, it is easy to show that I_D is constant in z and given by

$$\begin{aligned} I_D &= \sum_{i=1}^N \int_{-\infty}^{\infty} dx \int_{-\infty}^{\infty} dy \frac{\partial}{\partial t} \left(\frac{\sigma_i}{4\pi} \int_{-a/2}^{a/2} \int_{-b/2}^{b/2} dx' dy' \frac{z - z_i}{[(x - x')^2 + (y - y')^2 + (z - z'_i)^2]^{3/2}} \right) \\ &= \sum_{i=1}^N \frac{\partial}{\partial t} \left(\frac{\sigma_i}{4\pi} \int_{-a/2}^{a/2} \int_{-b/2}^{b/2} dx' dy' \frac{z - z_i}{[(x - x')^2 + (y - y')^2 + (z - z'_i)^2]^{3/2}} \right) \\ &= ab \sum_{i=1}^N \int_{-\infty}^{\infty} dx_1 \int_{-\infty}^{\infty} dy_1 \frac{\partial}{\partial t} \left(\frac{\sigma_i}{4\pi} \frac{z - z_i}{[x_1^2 + y_1^2 + (z - z'_i)^2]^{3/2}} \right). \end{aligned} \tag{17}$$

In obtaining the third equality, the substitution of variables x, y by $x_1 = x - x', y_1 = y - y'$ was used. Thus, the displacement current of the CS mode TENG is given by

$$\begin{aligned}
 I_D &= \int_s \frac{\partial \mathbf{D}}{\partial t} \cdot \mathbf{n} dS = \int_s \frac{\partial D_z}{\partial t} dS \\
 &= -\frac{1}{4\pi} (z - z_1) \frac{\partial}{\partial t} \left[\sigma_U(t) \int_{-\infty}^{\infty} dx \int_{-\infty}^{\infty} dy \int_{-a/2}^{a/2} dx' \int_{-b/2}^{b/2} \frac{dy'}{[(x - x')^2 + (y - y')^2 + (z - z_1)^2]^{3/2}} \right] \\
 &\quad + \frac{\sigma_T}{4\pi} (z - z_2) \frac{\partial}{\partial t} \left[\int_{-\infty}^{\infty} dx \int_{-\infty}^{\infty} dy \int_{-a/2}^{a/2} dx' \int_{-b/2}^{b/2} \frac{dy'}{[(x - x')^2 + (y - y')^2 + (z - z_2)^2]^{3/2}} \right] \\
 &\quad - \frac{\sigma_T}{4\pi} (z - z_3) \frac{\partial}{\partial t} \left[\int_{-\infty}^{\infty} dx \int_{-\infty}^{\infty} dy \int_{-a/2}^{a/2} dx' \int_{-b/2}^{b/2} \frac{dy'}{[(x - x')^2 + (y - y')^2 + (z - z_3)^2]^{3/2}} \right] \\
 &\quad + \frac{1}{4\pi} (z - z_4) \frac{\partial}{\partial t} \left[\sigma_U(t) \int_{-\infty}^{\infty} dx \int_{-\infty}^{\infty} dy \int_{-a/2}^{a/2} dx' \int_{-b/2}^{b/2} \frac{dy'}{[(x - x')^2 + (y - y')^2 + (z - z_4)^2]^{3/2}} \right]. \tag{18}
 \end{aligned}$$

Finally, one finds^{4,45}

$$I_D = I = \frac{\partial q}{\partial t}. \tag{19}$$

3. General theory of the dimensional analysis from the 3D mathematical modeling

Dimensional analysis enables one to predict the behavior of large systems from a study of small-scale models. It also provides a useful cataloging system of physical quantities. Here, the method of dimensional analysis is introduced to study the quasi-electrostatic model and output performances of TENGs. From Eq. (11), the dimensionless electric potential at an arbitrary point $\mathbf{r}^* = (x^*, y^*, z^*)$ is derived by⁴⁶

$$\begin{aligned}
 \phi^*(x^*, y^*, z^*) &= \sum_{i=1}^N \int_{-\frac{a}{2L}}^{\frac{a}{2L}} \int_{-\frac{b}{2M}}^{\frac{b}{2M}} LM\sigma_T \frac{\sigma_i^* dx'^* dy'^*}{4\pi\epsilon_0\epsilon(\mathbf{r}^*) \sqrt{L^2(x^* - x'^*)^2 + M^2(y^* - y'^*)^2 + N^2(z^* - z_i'^*)^2}} \\
 &= \sum_{i=1}^N \frac{LM\sigma_T\sigma_i^*}{4\pi\epsilon_0\epsilon(\mathbf{r}^*)} \int_{-\frac{a}{2L}}^{\frac{a}{2L}} \int_{-\frac{b}{2M}}^{\frac{b}{2M}} \frac{dx'^* dy'^*}{\sqrt{L^2(x^* - x'^*)^2 + M^2(y^* - y'^*)^2 + N^2(z^* - z_i'^*)^2}} \tag{20}
 \end{aligned}$$

and the related dimensionless electric field is

$$\begin{aligned}
 \mathbf{E}^*(x^*, y^*, z^*) &= -\nabla\phi^* \\
 &= \sum_{i=1}^N \frac{LM\sigma_T\sigma_i^*}{4\pi\epsilon_0\epsilon(\mathbf{r}^*)} \int_{-\frac{a}{2L}}^{\frac{a}{2L}} \int_{-\frac{b}{2M}}^{\frac{b}{2M}} \frac{dx'^* dy'^*}{\sqrt{L^2(x^* - x'^*)^2 + M^2(y^* - y'^*)^2 + N^2(z^* - z_i'^*)^2}} \frac{(x^* - x'^*, y^* - y'^*, z^* - z_i'^*)}{\sqrt{L^2(x^* - x'^*)^2 + M^2(y^* - y'^*)^2 + N^2(z^* - z_i'^*)^2}}, \tag{21}
 \end{aligned}$$

where $x^* = x/L, y^* = y/L, z^* = z/N$; and $x'^* = x'/L, y'^* = y'/L, z_i'^* = z_i'/L$; $\epsilon(\mathbf{r}^*) = \epsilon(\mathbf{r})/\epsilon_0, \sigma_i^* = \sigma_i/\Sigma\sigma_T$. L, M , and N are characteristic dimensions of the 3D mathematical model in the x, y , and z directions. Observe that L, M , and N are, in general, different. However, if $L = M = N$, these equations can be further simplified.⁴⁶

C. Power generation of TENGs

1. Power generation of the contact-separation (CS) mode TENG

Through Maxwell's equations, the 3D mathematical model of TENGs has been built. The advantages in using this quasi-electrostatic model are that it does not only provide a physical picture of the operation of TENGs, but also provides a time-dependent and complete 3D space resolution. A typical CS model TENG composed by two electrodes and two different dielectric materials are demonstrated in Fig. 6(c). According to the 3D mathematical model and Eq. (11), the electric potentials of the electrodes at $z = z_4$ and $z = z_1$ are given by⁴

$$\phi(0, 0, z_4) = -\frac{\sigma_U}{\pi\epsilon_2} \int_{z_4-z_1}^{\infty} f(z')dz' + \frac{\sigma_U}{\pi\epsilon_2} \int_0^{\infty} f(z')dz' + \frac{\sigma_T}{\pi\epsilon_2} \int_{z_4-z_2}^{\infty} f(z')dz' - \frac{\sigma_T}{\pi\epsilon_2} \int_{z_4-z_3}^{\infty} f(z')dz', \quad (22.a)$$

$$\phi(0, 0, z_1) = -\frac{\sigma_U}{\pi\epsilon_1} \int_0^{\infty} f(z')dz' + \frac{\sigma_U}{\pi\epsilon_1} \int_{z_1-z_4}^{\infty} f(z')dz' + \frac{\sigma_T}{\pi\epsilon_1} \int_{z_1-z_2}^{\infty} f(z')dz' - \frac{\sigma_T}{\pi\epsilon_1} \int_{z_1-z_3}^{\infty} f(z')dz', \quad (22.b)$$

where

$$f(z) = \arctan \left(\frac{ab}{4z\sqrt{\left(\frac{a}{2}\right)^2 + \left(\frac{b}{2}\right)^2 + z^2}} \right). \quad (23)$$

When a load resistance Z is connected between the electrodes, the voltage across Z is

$$\Delta V = ZI = -Z \frac{dQ}{dt} = -ZS \frac{d\sigma_U}{dt}, \quad (24)$$

where S is the area of the electrode which is equal to the contacting surface. According to Kirchhoff's law,

$$-ZS \frac{d\sigma_U}{dt} = \phi(0, 0, z_4) - \phi(0, 0, z_1). \quad (25)$$

This equation is essentially the same as Eq. (7), both of them are first-order linear differential equations. By solving Eq. (25), the charge density, current, voltage as well as the transient power P can be determined. The electrical energy E is calculated as the integral of transient power P . As stated above, the extracted electrical energy is determined by the conditioning circuit of the TENG device.

Furthermore, the open-circuit voltage V_{OC} and short-circuit current I_{SC} are given by

$$-V_{OC} = \phi(0, 0, z_4) - \phi(0, 0, z_1) = \frac{\sigma_T}{\pi\epsilon_2} \int_{z_4-z_2}^{z_4-z_3} f(z')dz' + \frac{\sigma_T}{\pi\epsilon_1} \int_{z_1-z_3}^{z_1-z_2} f(z')dz', \quad (26)$$

$$I_{SC} = S \frac{d\sigma_U}{dt}. \quad (27)$$

The numerical results of V_{OC} and Q_{SC} as well as I_{SC} calculated from different models are illustrated in Fig. 7, in which the method of FSCP modeling (finite-sized-charged planes) is equal to the method of 3D mathematical modeling. It is seen that the methods of 3D modeling and DDEF modeling lead to the same result, but the CA model exhibits markedly different results especially at a larger relative movement.^{4,47} This difference is a result of finite-edge effects not accounted for in the CA model.

Based on this quasi-electrostatic model, a time-domain variation of the CS mode TENG with inductive load has also been modeled. Figures 8(a) and 8(b) show a basic structure of a CS

model TENG and it is connected with an inductive circuit, respectively. From Eq. (11), the electric potentials at each electrode are⁴⁹

$$\begin{aligned} \varphi_a = & -\frac{\rho_{ab}}{\pi\epsilon_a} \int_{D_a+D_b+d(t)}^{\infty} f(z)dz + \frac{\rho_{ab}}{\pi\epsilon_a} \int_0^{\infty} f(z)dz \\ & + \frac{\rho_\epsilon}{\pi\epsilon_a} \int_{D_a+d(t)}^{\infty} f(z)dz - \frac{\rho_\epsilon}{\pi\epsilon_a} \int_{D_a}^{\infty} f(z)dz, \end{aligned} \quad (28.a)$$

$$\begin{aligned} \varphi_b = & -\frac{\rho_{ab}}{\pi\epsilon_b} \int_0^{\infty} f(z)dz + \frac{\rho_{ab}}{\pi\epsilon_b} \int_{-D_a-D_b-d(t)}^{\infty} f(z)dz \\ & + \frac{\rho_\epsilon}{\pi\epsilon_b} \int_{-D_b}^{\infty} f(z)dz - \frac{\rho_\epsilon}{\pi\epsilon_b} \int_{-D_b-d(t)}^{\infty} f(z)dz. \end{aligned} \quad (28.b)$$

The potential difference is written as

$$V_{ab} = RI + L \frac{dI}{dt} = -R \frac{dQ}{dt} - L \frac{d^2Q}{dt^2} = -RS \frac{d\rho_{ab}}{dt} - LS \frac{d^2\rho_{ab}}{dt^2}, \quad (29)$$

where R is the system inductance and I denotes the current flowing the circuit. Kirchhoff's law states

$$-LS \frac{d^2\rho_{ab}}{dt^2} - RS \frac{d\rho_{ab}}{dt} = \varphi_a - \varphi_b. \quad (30)$$

Unlike Eq. (25), the latter equation is a second-order ordinary differential equation (ODE). Its solution provides the time-domain free charge density on the electrode. Note that the initial condition is $\rho_{ab} = 0$. The power output from the CS mode TENG is

$$\begin{aligned} P_t(t) = & V_{ab}(t)I(t) = RI^2(t) + LI(t) \frac{dI(t)}{dt} \\ = & RS^2 \left(\frac{d\rho_{ab}}{dt} \right) + LS \frac{d\rho_{ab}}{dt} \frac{d^2\rho_{ab}}{dt^2}. \end{aligned} \quad (31)$$

Figures 8(c)–8(f) demonstrate the basic outputs of this energy oscillation circuit. As seen from Fig. 8(c) and 8(d), for a low-resistive load, a higher peak and longer periods of oscillation are found. However, only weak or even no oscillations are obtained for the time-domain voltage curve for a large load resistor. A similar trend is observed for the total power output [Figs. 8(e) and 8(f)]. Note that because of the phase shift difference between the current and voltage of the inductor, a negative value in the total power is obtained. In

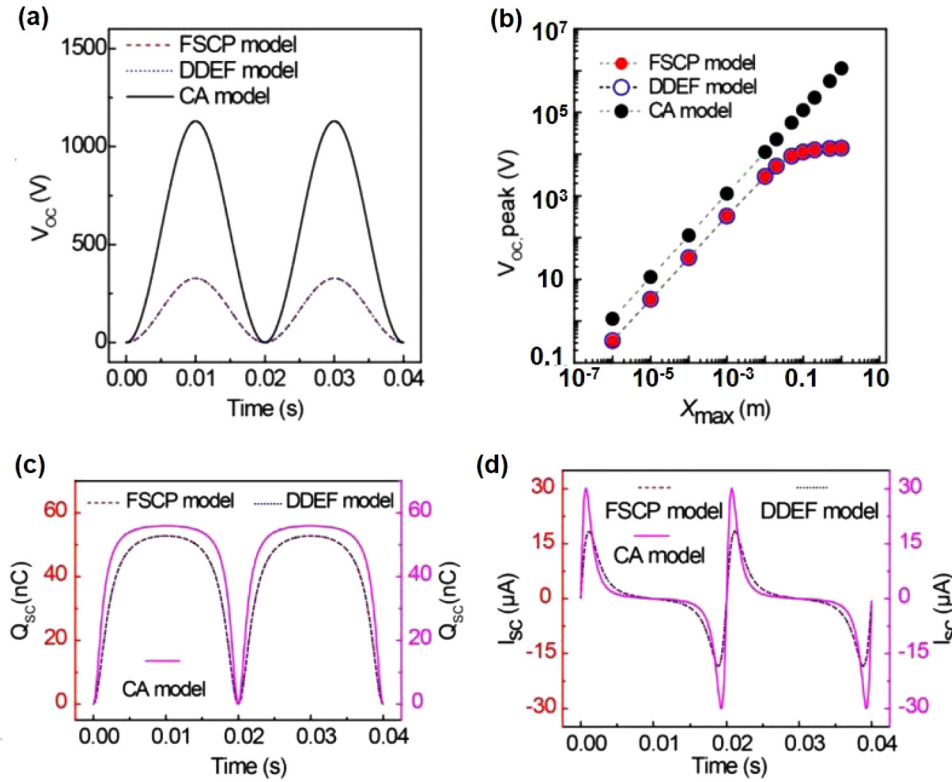


FIG. 7. Comparisons of basic outputs for the vertical contact-separation mode TENG among the finite-sized charges plane (FSCP) model (also called as three-dimensional mathematical model), distance-dependent electric field (DDEF) model and the capacitive (CA) mode of TENGs. (a) Open-circuit voltage (V_{oc})–time relationship; (b) peak of open-circuit voltage at different maximum contact-separation distance (X_{max}); (c) short-circuit output charges (Q_{sc})–time relationship; (d) corresponding short-circuit current (I_{sc})–time relationship.⁴ Reproduced with permission from Shao *et al.*, *Nano Energy* **60**, 630 (2019). Copyright 2019 Elsevier.

general, the positive (or negative) oscillating value of the total power corresponds to storing (or releasing of the stored) energy in the inductor. Instead, a similar tendency with unidirectional (i.e., always positive) oscillations is found for the time-domain power output on the load; especially when the load resistance is small. Compared with the total power depicted in Figs. 8(e) and 8(f), the power through the load is extremely weak. The inductor is a pure energy oscillation operation while the load is consuming the energy. Many research works have proposed special circuits employing a combination of an inductor and other types of circuit blocks.

2. Power generation of the single-electrode contact (SEC) mode TENG

Figure 6(d) illustrates a typical SEC mode TENG, composed by one dielectric film and two electrodes. One electrode is regarded as the primary electrode while the other is the reference electrode. When the dielectric film moves up and down, the potential difference drives the electrons to move from one electrode to the other, leading to the generation of a conduction current. Using the method of 3D mathematical modeling, the electric field component perpendicular to the charged planes (along the z direction) of the SEC model is written as⁴

$$E_z(0, 0, z) = \frac{\sigma_U}{\pi\epsilon_0} f(z - z_1) - \frac{\sigma_U}{\pi\epsilon_0} f(z - z_2) + \frac{\sigma_T}{\pi\epsilon_0} f(z - z_2) - \frac{\sigma_T}{\pi\epsilon_0} f(z - z_3). \quad (32)$$

In the same way, the electric potentials at the positions of z_1 and z_4 read

$$\phi(0, 0, z_1) = \frac{\sigma_U}{\pi\epsilon_0} \int_0^\infty f(z') dz' - \frac{\sigma_U}{\pi\epsilon_0} \int_{z_1-z_2}^\infty f(z') dz' + \frac{\sigma_T}{\pi\epsilon_0} \int_{z_1-z_2}^\infty f(z') dz' - \frac{\sigma_T}{\pi\epsilon_0} \int_{z_1-z_3}^\infty f(z') dz', \quad (33.a)$$

$$\phi(0, 0, z_2) = \frac{\sigma_U}{\pi\epsilon_0} \int_{z_2-z_1}^\infty f(z') dz' - \frac{\sigma_U}{\pi\epsilon_0} \int_0^\infty f(z') dz' + \frac{\sigma_T}{\pi\epsilon_0} \int_0^\infty f(z') dz' - \frac{\sigma_T}{\pi\epsilon_0} \int_{z_2-z_3}^\infty f(z') dz'. \quad (33.b)$$

From Eq. (7), the voltage across a connected load Z implies

$$\Delta\phi = -ZS \frac{d\sigma_U}{dt}, \quad (34)$$

where $\Delta\phi$ stands for the potential difference between the two electrodes.

The electric potential and potential difference–time relationships with various load resistances of the SEC mode TENG are numerically calculated and shown in Figs. 9(a) and 9(b). The electric potential at positions $z = z_1$ and $z = z_4$ are denoted by ϕ_a and ϕ_b , respectively. The encircled areas of electric potential-

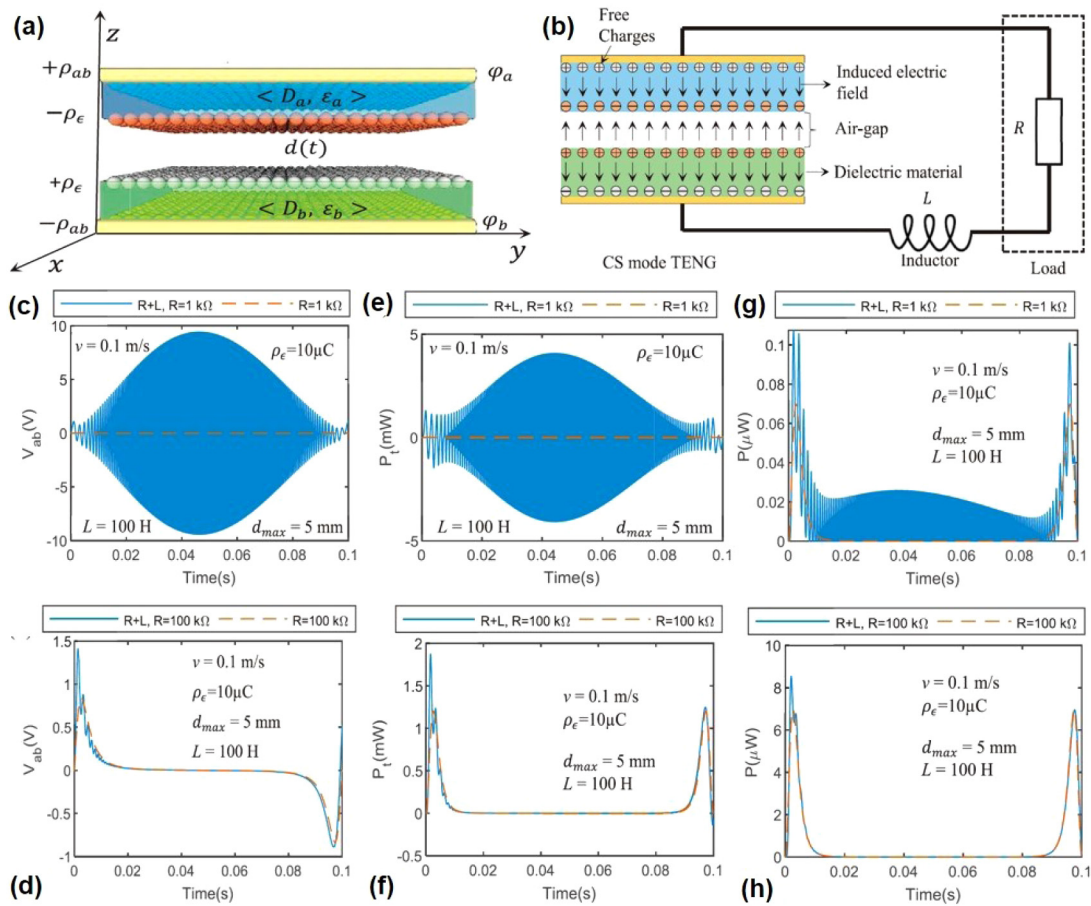


FIG. 8. Output characteristics of the vertical contact-separation mode TENG connected to the oscillation circuit. (a) The structure of the vertical contact-separation mode TENG; (b) vertical contact-separation mode TENG with the connection of an external inductor and load; voltage–time relationship (c), total power–time relationship (e) and power to the load–time relationship (g) for the vertical contact-separation mode TENG connected to the external load of $R = 1\text{ k}\Omega$ and $L = 100\text{ H}$; voltage–time relationship (d), total power–time relationship (f) and power to the load–time relationship (h) for the vertical contact-separation mode TENG connected to the external load of $R = 100\text{ k}\Omega$ and $L = 100\text{ H}$.⁴⁹ Reproduced with permission from Lu et al., Nano Energy **63**, 103883 (2019). Copyright 2019 Elsevier.

transferred charge curves [Fig. 9(c)] are equivalent to the extracted electrical energy, from which it is found that the harvested energy increases with the increasing of the load resistance. The electric field at positions of z_1 , z_3 and corresponding displacement current are depicted in Figs. 9(d)–9(i). Numerical simulations are carried out according to Eqs. (14) and (22). The normal fluctuation range of the electric field at z_1 is larger than that of the electric field at z_3 . This is because the air gap (h) between the two electrodes is very small ($h = 0.01\text{ m}$). Thus, the electric field due to surface charges at z_3 strongly affects the charge transformation between z_1 and z_2 . When h increases [Figs. 9(g)–9(i)], the electric field contribution from z_3 decreases and the total electric field at z_1 changes in a reversible manner. At this position, if the maximum z becomes large enough, the electric field contribution from z_3 has little influence at positions

z_1 and z_2 , and the saturated transferred charge density σ_u will be just half the value of σ_T .^{4,50} The corresponding I_D calculated from Eq. (18) is shown in Fig. 9(f).

3. Power generation of the lateral-sliding (LS) mode TENG

As stated above, another advantage of the method of 3D mathematical modeling is that it creates a time-dependent 3D space resolution. For example, this model has been used to predict the output performance of the LS model TENG, whose moving part moves in the horizontal direction but not in the vertical direction. A typical LS model TENG composed of two dielectric films and electrodes is depicted in Fig. 6(e). When there is a relative movement, tribocharges are produced at the contacting surfaces. At

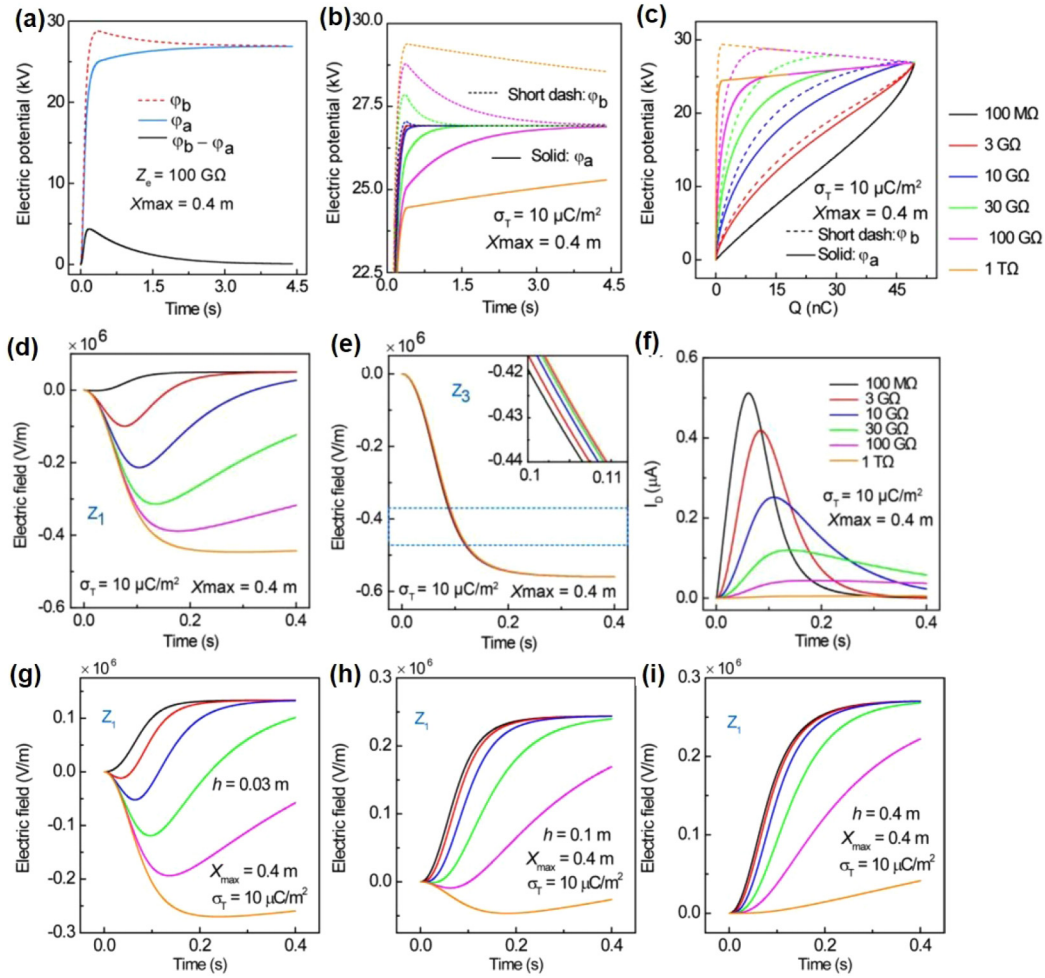


FIG. 9. Electric potential and electric field of the single-electrode mode TENG numerically calculated based on the three-dimensional mathematical mode. (a) Electric potential and potential difference–time relationship with the load resistance of 100 GΩ; (b) electric potential–time relationships at different load resistances; (c) electric potential–output charge plots at different load resistances; electric field–time relationships at the positions of $z = z_1$ (d, g, h, i) and (e) $z = z_3$, and (f) corresponding displacement current at different load resistances. The quantity h represents the separation distance of between z_1 and z_3 for the single-electrode mode TENG.⁴ Reproduced with permission from Shao *et al.*, *Nano Energy* **60**, 630 (2019). Copyright 2019 Elsevier.

the overlapping areas of the dielectric film, tribocharges are zero since the distance between the two contacting surfaces is extremely small under ideal condition.^{46,51}

According to the 3D mathematical model and Eq. (11), the electric potential of the LS mode TENG at OC conditions can be rewritten as⁴⁶

$$\begin{aligned} \phi(x, y, z, t) = & -\frac{\sigma_T}{4\pi\epsilon(\mathbf{r})} \int_0^{a(t)} dx' \int_{-b/2}^{b/2} \frac{dy'}{[(x-x')^2 + (y-y')^2 + (z-z_0)^2]^{1/2}} + \frac{\sigma_T}{4\pi\epsilon(\mathbf{r})} \int_L^{L+a(t)} dx' \int_{-b/2}^{b/2} \frac{dy'}{[(x-x')^2 + (y-y')^2 + (z-z_0)^2]^{1/2}} \\ & + \frac{\sigma_T}{4\pi\epsilon(\mathbf{r})} \int_0^{a(t)} dx' \int_{-b/2}^{b/2} \frac{dy'}{[(x-x')^2 + (y-y')^2 + (z-z_1)^2]^{1/2}} - \frac{\sigma_T}{4\pi\epsilon(\mathbf{r})} \int_L^{L+a(t)} dx' \int_{-b/2}^{b/2} \frac{dy'}{[(x-x')^2 + (y-y')^2 + (z-z_2)^2]^{1/2}} \\ & + \frac{\sigma_E}{4\pi\epsilon(\mathbf{r})} \int_{a(t)}^L dx' \int_{-b/2}^{b/2} \frac{dy'}{[(x-x')^2 + (y-y')^2 + (z-z_3)^2]^{1/2}} - \frac{\sigma_E}{4\pi\epsilon(\mathbf{r})} \int_{a(t)}^L dx' \int_{-b/2}^{b/2} \frac{dy'}{[(x-x')^2 + (y-y')^2 + (z-z_4)^2]^{1/2}}, \end{aligned} \quad (35)$$

where $a(t)$ is a relative time-dependent distance and L represents the length of the electrode. σ_E is the charge density existing at the overlapping part of the bottom (top) electrode, which is determined by the requirement that the charge density σ_0 on the electrodes must be zero at any time. Here, the notation z_{0-} indicates that negative tribocharges are generated at a z value infinitesimally smaller than z_0 . Furthermore, z_{0+} implies that positive tribocharges are generated at a z value infinitesimally larger than z_0 . The corresponding electric field at OC conditions is

$$\begin{aligned}
 E(x, y, z, t) = & -\frac{\sigma_T}{4\pi\epsilon(\mathbf{r})} \int_0^{a(t)} dx' \int_{-b/2}^{b/2} \frac{(x-x', y-y', z-z_{0-})}{[(x-x')^2+(y-y')^2+(z-z_{0-})^2]^{3/2}} dy' + \frac{\sigma_T}{4\pi\epsilon(\mathbf{r})} \int_L^{L+a(t)} dx' \int_{-b/2}^{b/2} \frac{(x-x', y-y', z-z_{0+})}{[(x-x')^2+(y-y')^2+(z-z_{0+})^2]^{3/2}} dy' \\
 & + \frac{\sigma_T}{4\pi\epsilon(\mathbf{r})} \int_0^{a(t)} dx' \int_{-b/2}^{b/2} \frac{(x-x', y-y', z-z_1)}{[(x-x')^2+(y-y')^2+(z-z_1)^2]^{3/2}} dy' - \frac{\sigma_T}{4\pi\epsilon(\mathbf{r})} \int_L^{L+a(t)} dx' \int_{-b/2}^{b/2} \frac{(x-x', y-y', z-z_2)}{[(x-x')^2+(y-y')^2+(z-z_2)^2]^{3/2}} dy' \\
 & + \frac{\sigma_E}{4\pi\epsilon(\mathbf{r})} \int_{a(t)}^L dx' \int_{-b/2}^{b/2} \frac{(x-x', y-y', z-z_1)}{[(x-x')^2+(y-y')^2+(z-z_1)^2]^{3/2}} dy' - \frac{\sigma_E}{4\pi\epsilon(\mathbf{r})} \int_{a(t)}^L dx' \int_{-b/2}^{b/2} \frac{(x-x', y-y', z-z_2)}{[(x-x')^2+(y-y')^2+(z-z_2)^2]^{3/2}} dy'.
 \end{aligned} \tag{36}$$

According to the definition of displacement current and Eq. (12), the displacement current through the internal TENG surface z at OC conditions ($I_{D,OC}$) is

$$\begin{aligned}
 I_{D,OC} = & \int_s \frac{\partial \mathbf{D}}{\partial t} \cdot \mathbf{n} dS = \int_s \frac{\partial D_z}{\partial t} dS \\
 = & +\frac{\sigma_T}{4\pi} (z+z_{0-}) \frac{\partial}{\partial t} \left(\int_{-\infty}^{\infty} dx \int_{-\infty}^{\infty} dy \int_0^{a(t)} dx' \int_{-b/2}^{b/2} \frac{dy'}{[(x-x')^2+(y-y')^2+(z-z_{0-})^2]^{3/2}} \right) \\
 & -\frac{\sigma_T}{4\pi} (z-z_{0+}) \frac{\partial}{\partial t} \left(\int_{-\infty}^{\infty} dx \int_{-\infty}^{\infty} dy \int_L^{L+a(t)} dx' \int_{-b/2}^{b/2} \frac{dy'}{[(x-x')^2+(y-y')^2+(z-z_{0+})^2]^{3/2}} \right) \\
 & -\frac{\sigma_T}{4\pi} (z-z_1) \frac{\partial}{\partial t} \left(\int_{-\infty}^{\infty} dx \int_{-\infty}^{\infty} dy \int_0^{a(t)} dx' \int_{-b/2}^{b/2} \frac{dy'}{[(x-x')^2+(y-y')^2+(z-z_1)^2]^{3/2}} \right) \\
 & +\frac{\sigma_T}{4\pi} (z+z_2) \frac{\partial}{\partial t} \left(\int_{-\infty}^{\infty} dx \int_{-\infty}^{\infty} dy \int_L^{L+a(t)} dx' \int_{-b/2}^{b/2} \frac{dy'}{[(x-x')^2+(y-y')^2+(z-z_2)^2]^{3/2}} \right) \\
 & -\frac{1}{4\pi} (z-z_1) \frac{\partial}{\partial t} \left(\sigma_E(t) \int_{-\infty}^{\infty} dx \int_{-\infty}^{\infty} dy \int_{a(t)}^L dx' \int_{-b/2}^{b/2} \frac{dy'}{[(x-x')^2+(y-y')^2+(z-z_1)^2]^{3/2}} \right) \\
 & +\frac{1}{4\pi} (z+z_2) \frac{\partial}{\partial t} \left(\sigma_E(t) \int_{-\infty}^{\infty} dx \int_{-\infty}^{\infty} dy \int_{a(t)}^L dx' \int_{-b/2}^{b/2} \frac{dy'}{[(x-x')^2+(y-y')^2+(z-z_2)^2]^{3/2}} \right).
 \end{aligned} \tag{37}$$

Using the same method, the electric field at SC conditions is

$$\begin{aligned}
 E(x, y, z, t) = & -\frac{\sigma_T}{4\pi\epsilon(\mathbf{r})} \int_0^{a(t)} dx' \int_{-b/2}^{b/2} dy' \frac{(x-x', y-y', z-z_{0-})}{[(x-x')^2+(y-y')^2+(z-z_{0-})^2]^{3/2}} \\
 & +\frac{\sigma_T}{4\pi\epsilon(\mathbf{r})} \int_L^{L+a(t)} dx' \int_{-b/2}^{b/2} dy' \frac{(x-x', y-y', z-z_{0+})}{[(x-x')^2+(y-y')^2+(z-z_{0+})^2]^{3/2}} + \frac{\sigma_T}{4\pi\epsilon(\mathbf{r})} \int_0^{a(t)} dx' \int_{-b/2}^{b/2} dy' \frac{(x-x', y-y', z-z_1)}{[(x-x')^2+(y-y')^2+(z-z_1)^2]^{3/2}} \\
 & -\frac{\sigma_T}{4\pi\epsilon(\mathbf{r})} \int_L^{L+a(t)} dx' \int_{-b/2}^{b/2} dy' \frac{(x-x', y-y', z-z_2)}{[(x-x')^2+(y-y')^2+(z-z_2)^2]^{3/2}} + \frac{\sigma_E}{4\pi\epsilon(\mathbf{r})} \int_{a(t)}^L dx' \int_{-b/2}^{b/2} dy' \frac{(x-x', y-y', z-z_1)}{[(x-x')^2+(y-y')^2+(z-z_1)^2]^{3/2}} \\
 & -\frac{\sigma_E}{4\pi\epsilon(\mathbf{r})} \int_{a(t)}^L dx' \int_{-b/2}^{b/2} dy' \frac{(x-x', y-y', z-z_2)}{[(x-x')^2+(y-y')^2+(z-z_2)^2]^{3/2}} + \frac{\sigma_U}{4\pi\epsilon(\mathbf{r})} \int_{a(t)}^L dx' \int_{-b/2}^{b/2} dy' \frac{(x-x', y-y', z-z_1)}{[(x-x')^2+(y-y')^2+(z-z_1)^2]^{3/2}} \\
 & -\frac{\sigma_U}{4\pi\epsilon(\mathbf{r})} \int_{a(t)}^L dx' \int_{-b/2}^{b/2} dy' \frac{(x-x', y-y', z-z_2)}{[(x-x')^2+(y-y')^2+(z-z_2)^2]^{3/2}}.
 \end{aligned} \tag{38}$$

Note that to maintain electrostatic equilibrium, charges will be transferred from one electrode to the other at SC conditions. The transferred charges are represented by $\pm\sigma_U(t)$, respectively. Then, the relevant displacement current through the entire surface z at SC conditions ($I_{D,SC}$) is

$$\begin{aligned}
 I_{D,SC} &= \int_s \frac{\partial \mathbf{D}}{\partial t} \cdot \mathbf{n} dS = \int_s \frac{\partial D_z}{\partial t} dS \\
 &= -\frac{\sigma_T}{4\pi} (z - z_0^-) \frac{\partial}{\partial t} \left(\int_{-\infty}^{\infty} dx \int_{-\infty}^{\infty} dy \int_0^{a(t)} dx' \int_{-b/2}^{b/2} \frac{dy'}{[(x - x')^2 + (y - y')^2 + (z - z_0^-)^2]^{3/2}} \right) \\
 &\quad + \frac{\sigma_T}{4\pi} (z - z_0^+) \frac{\partial}{\partial t} \left(\int_{-\infty}^{\infty} dx \int_{-\infty}^{\infty} dy \int_L^{L+a(t)} dx' \int_{-b/2}^{b/2} \frac{dy'}{[(x - x')^2 + (y - y')^2 + (z - z_0^+)^2]^{3/2}} \right) \\
 &\quad + \frac{\sigma_T}{4\pi} (z - z_1) \frac{\partial}{\partial t} \left(\int_{-\infty}^{\infty} dx \int_{-\infty}^{\infty} dy \int_0^{a(t)} dx' \int_{-b/2}^{b/2} \frac{dy'}{[(x - x')^2 + (y - y')^2 + (z - z_1)^2]^{3/2}} \right) \\
 &\quad - \frac{\sigma_T}{4\pi} (z - z_2) \frac{\partial}{\partial t} \left(\int_{-\infty}^{\infty} dx \int_{-\infty}^{\infty} dy \int_L^{L+a(t)} dx' \int_{-b/2}^{b/2} \frac{dy'}{[(x - x')^2 + (y - y')^2 + (z - z_2)^2]^{3/2}} \right) \\
 &\quad - \frac{\sigma_E}{4\pi} (z - z_1) \frac{\partial}{\partial t} \left(\int_{-\infty}^{\infty} dx \int_{-\infty}^{\infty} dy \int_{a(t)}^L dx' \int_{-b/2}^{b/2} \frac{dy'}{[(x - x')^2 + (y - y')^2 + (z - z_1)^2]^{3/2}} \right) \\
 &\quad + \frac{\sigma_E}{4\pi} (z - z_2) \frac{\partial}{\partial t} \left(\int_{-\infty}^{\infty} dx \int_{-\infty}^{\infty} dy \int_{a(t)}^L dx' \int_{-b/2}^{b/2} \frac{dy'}{[(x - x')^2 + (y - y')^2 + (z - z_2)^2]^{3/2}} \right) \\
 &\quad + \frac{\sigma_U}{4\pi} (z - z_1) \frac{\partial}{\partial t} \left(\int_{-\infty}^{\infty} dx \int_{-\infty}^{\infty} dy \int_{a(t)}^L dx' \int_{-b/2}^{b/2} \frac{dy'}{[(x - x')^2 + (y - y')^2 + (z - z_1)^2]^{3/2}} \right) \\
 &\quad - \frac{\sigma_U}{4\pi} (z - z_2) \frac{\partial}{\partial t} \left(\int_{-\infty}^{\infty} dx \int_{-\infty}^{\infty} dy \int_{a(t)}^L dx' \int_{-b/2}^{b/2} \frac{dy'}{[(x - x')^2 + (y - y')^2 + (z - z_2)^2]^{3/2}} \right). \tag{39}
 \end{aligned}$$

If a load resistor is connected between the two electrodes, the electrical potential at the positions of z_1 and z_2 are given by $\phi_1(x, y, z_1, t)$ and $\phi_2(x, y, z_2, t)$, respectively. The governing equation of the LS model TENG is written as

$$-ZS \frac{d\sigma_U}{dt} = \phi_1(x, y, z_1) - \phi_2(x, y, z_2). \tag{40}$$

Note that Z represents the external electric impedance and S is the contacting surface. As mentioned earlier, Eq. (40) is a time-dependent differential equation, through which $\sigma_U(t)$ can be solved. Furthermore, the current, transient power, electrical energy, and average power of the LS mode TENG can be predicted.

It was demonstrated that the TENG transducer couples the mechanical and electrical energy fields. The mechanical energy is first converted into electrical energy and stored in the TENG device through the presence of an electric field, and a part of the electrical energy is extracted to the external circuit. The magnitude of the extracted energy or electrical energy is controlled by the conditioning circuit. On the other hand, according to the built capacitive model, the TENG device is represented by an open-circuit voltage (V_{OC}) source in series with a time-varying capacitor [$C(t)$]. The TENG, due to its time-varying capacitor, serves as a resistance to the flow of electric charges, and is represented by an internal resistance is [$Z_T(t)$] is defined by⁴⁶

$$Z_T(t) \equiv \frac{1}{\omega C(t)} = \frac{1}{2\pi f C(t)}, \tag{41}$$

where ω is the angular velocity and f is the frequency. In general, only when an external load is equal to the internal resistance of the TENG device, the largest electrical energy is obtained. The corresponding external load is denoted as the optimum resistance. However, due to the internal resistance of a TENG changing in time (except for the free-standing model TENG), its effective value [root mean square (*rms*)] is utilized to get the optimum resistor. The *rms* value/effective value of $Z_T(t)$ is defined by⁴⁶

$$Z_{opt} = Z_{rms} = \sqrt{\frac{1}{T} \int_0^T [Z_T(t)]^2 dt}, \tag{42}$$

where T stands for the period of $Z_T(t)$. If the *rms* of an AC signal has the same value as a DC signal then the two signals dissipate the same amount of power. Hence, Z_{rms} can be regarded as the optimum resistance of a TENG device. Through the same method, the *rms*/effective voltage (V_{rms}), current (I_{rms}), and charge (Q_{rms}) are finally derived. It can be shown that the relationship among the average power (P_{av}), V_{rms} and I_{rms} is⁴⁶

$$P_{av} = V_{rms} I_{rms}. \tag{43}$$

Equation (43) is the power transfer in a full cycle. Numerical simulations of the LS mode TENG are illustrated in Figs. 10(a)–10(e). Figure 10(f) shows a comparison of the average power calculated for two different optimum resistances. The P_{av} for the optimum resistance in steady state ($Z_{opt,steady}$) is $26.65 \mu\text{W}$, which is improved by a factor of 77.5% when compared to that of at the optimum resistance calculated from the transition state ($Z_{opt,1half}$).⁴⁶ The optimum resistance of a TENG device is obtained from Eq. (42). To compare performances, the *rms* voltage and current as well as the average power are relevant.

Based on the quasi-electrostatic model, theoretical models of the CS mode TENG, SEC mode TENG, and LS mode TENG have been developed. It can be predicted that the method of 3D modeling built from the quasi-electrostatic model is also available to other kinds of TENGs such as the freestanding mode TENG or other harvesters that are governed by the displacement current. In other words, as a general model, the quasi-electrostatic model can not only clarify the physical picture of a TENG device, but also predict the output characteristics of the TENGs.

D. Quasi-electrostatic model of TENGs: distance-dependent electric field (DDEF) modeling

1. Electric field of TENGs calculated by the DDEF model

As stated above, the method of 3D mathematical modeling is proposed based on the quasi-electrostatic model, which can be utilized to describe the variations in the 3D structure. In fact, the method of DDEF modeling is a special case of the 3D mathematical modeling, useful only to explore the variation in one particular direction. As demonstrated in Fig. 11(a), consider a charged triboelectric layer with dimensions L and W , uniform surface charge density of σ , in a free space with the permittivity of ϵ_0 , the electric field perpendicular to the layer (E_z) is^{47,48,52}

$$E_z = \frac{\sigma}{\pi\epsilon_0} \arctan \left(\frac{\frac{L}{W}}{2\left(\frac{z}{W}\right)\sqrt{4\left(\frac{z}{W}\right)^2 + \left(\frac{L}{W}\right)^2 + 1}} \right) = \frac{\sigma}{\pi\epsilon_0} f(z). \quad (44)$$

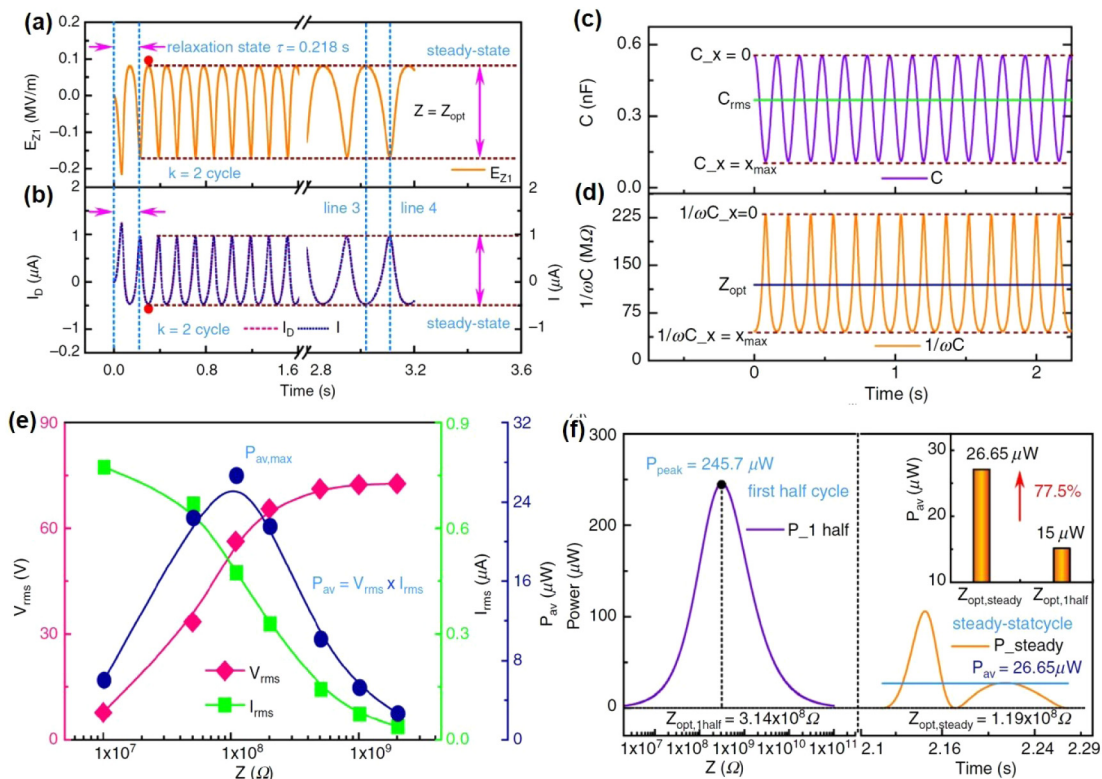


FIG. 10. Output characteristics of the lateral-sliding mode TENG. (a) Electric field at the bottom electrode ($z = z_1$) and (b) corresponding displacement current vs time at the optimum resistance; (c) capacitance and (d) reactance vs time under periodic mechanical motion of the single-electrode mode TENG; C_{rms} represents the root-mean square capacitance; (e) root-mean square voltage (V_{rms}), current (I_{rms}), and average power (P_{av}) at different load resistances; (f) a comparison of maximum average power P_{av} between the two different optimum resistances: the first one ($Z_{opt,1half}$) comes from the transient state (the first half-cycle), and the second one ($Z_{opt,steady}$) from the steady state.⁴⁶ Reproduced with permission from Shao *et al.*, Appl. Phys. Rev. 7, 011405 (2020). Copyright 2020 AIP Publishing LLC.

Considering two opposite tribocharged surfaces, the total electric field can be rewritten as

$$E_{\text{Total}} = \frac{\sigma}{\pi\epsilon_0} [f(x) - f(x+z)], \quad (45)$$

where z is the separation distance between the two charged layers, and x represents the distance from the point of interest to the charged layers. The total electric field at the midpoint of a convex charged surface is [Fig. 11(b)]⁴⁷

$$E_{z,\text{convex}} = \frac{\sigma L}{\pi\epsilon_0} \int_0^{w/2} \frac{\left(z + \frac{w}{2} - \sqrt{\frac{w^2}{2} - x^2}\right)}{R_1^2 \sqrt{4R_1^2 + L^2}} dx, \quad (46.a)$$

where

$$R_1^2 = x^2 + \left(z + \frac{w}{2} - \sqrt{\frac{w^2}{2} - x^2}\right)^2. \quad (46.b)$$

For a concaved charged layer, the electric field is⁴⁷

$$E_{z,\text{concave}} = \frac{\sigma L}{\pi\epsilon_0} \int_0^{w/2} \frac{\left(z - \frac{w}{2} + \sqrt{\frac{w^2}{4} - x^2}\right)}{R_2^2 \sqrt{4R_2^2 + L^2}} dx, \quad (47.a)$$

where

$$R_2^2 = x^2 + \left(z - \frac{w}{2} + \sqrt{\frac{w^2}{4} - x^2}\right)^2. \quad (47.b)$$

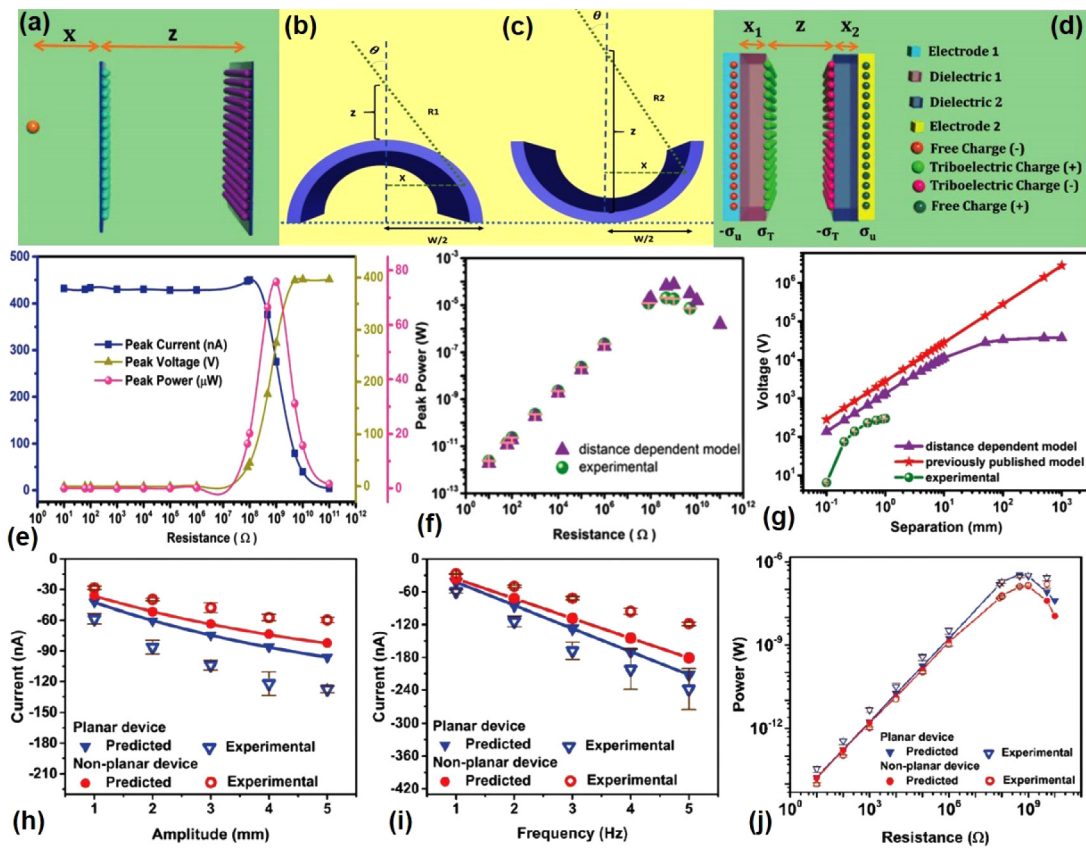


FIG. 11. Output characteristics of the vertical contact-separation mode TENG numerically calculated from the Distance-Dependent-Electric Field mode (DFEF model). (a) calculation of the total electric field originating from the two oppositely charged planes; calculating the total electric field originating from the (b) convex and (c) concave charged regions; (d) a typical contact-separation mode TENG with four charged layers; (e) three working regions of the contact-separation mode TENG at different load resistances; (f) a comparison of peak power between the theoretical and experimental results; (g) comparison of experimental open-circuit voltage vs theoretical results from the distance-dependent mode and capacitive mode (previously published mode); comparison of current between the numerical simulations and experimental results at different (h) amplitudes and (i) frequencies; (j) a comparison of the peak power at different load resistances.⁴⁷ Reproduced with permission from Dharmasena *et al.*, *Energy Environ. Sci.* **10**, 1801 (2017). Copyright 2017 Royal Society of Chemistry.

2. Electric potentials of TENGs calculated by the DDEF model

According to Eqs. (12) and (44), the electric field from the charged surface depends on σ_T and z of the TENG device. A special CS mode TENG with m tribocharged surfaces is shown in Fig. 11(j). Setting the zero point of the electric potential at infinity the electric potentials at electrode a (ϕ_a) and b (ϕ_b) are written as⁴⁸

$$\phi_a = -\frac{\sigma_U}{\pi\epsilon_a} \int_0^y f(x)dx + \frac{1}{\pi} \sum_{i=1}^m \left(\frac{\sigma_{T,i}}{\epsilon_a} \int_{x_{a,i}}^{\infty} f(x)dx \right), \quad (48.a)$$

$$\phi_b = -\frac{\sigma_U}{\pi\epsilon_b} \int_0^y f(x)dx + \frac{1}{\pi} \sum_{i=1}^m \left(\frac{\sigma_{T,i}}{\epsilon_b} \int_{x_{b,i}}^{\infty} f(x)dx \right). \quad (48.b)$$

From Eq. (7), the potential difference V between the two electrodes is

$$V = \phi_a - \phi_b, \quad (49)$$

When a load resistor Z is connected between the two electrodes, the voltage across Z is

$$LWZ \frac{d\sigma_U}{dt} + \frac{\sigma_U}{\pi} \left(\frac{1}{\epsilon_a} + \frac{1}{\epsilon_b} \right) \int_0^y f(x)dx - \frac{1}{\pi} \left[\sum_{i=1}^m \left(\frac{\sigma_{T,i}}{\epsilon_a} \int_{x_{a,i}}^{\infty} f(x)dx - \frac{\sigma_{T,i}}{\epsilon_b} \int_{x_{b,i}}^{\infty} f(x)dx \right) \right] = 0. \quad (50)$$

The latter is also a time-dependent differential equation that allows $\sigma_u(t)$ to be determined. As stated earlier, at OC conditions the transferred charge is zero, i.e., $\sigma_u(t) = 0$; while at SC conditions the potential difference is 0, i.e., $V = \phi_a - \phi_b = 0$.

E. Outputs characteristics of TENGs calculated by the DDEF model

1. Electrical potential of the CS mode TENG

A typical CS mode TENG is illustrated in Fig. 11(d). Using the method of DDEF modeling and Eq. (48), the electrical potentials at electrodes 1 and 2 are rewritten as⁴⁷

$$\phi_1 = -\frac{\sigma_U}{\pi\epsilon_1} \left[\int_0^{x_1+x_2+z} f(x)dx \right] + \frac{\sigma_T}{\pi\epsilon_1} \left[\int_{x_1}^{x_1+z} f(x)dx \right], \quad (51.a)$$

$$\phi_2 = -\frac{\sigma_U}{\pi\epsilon_2} \left[\int_0^{x_1+x_2+z} f(x)dx \right] - \frac{\sigma_T}{\pi\epsilon_2} \left[\int_{x_2}^{x_2+z} f(x)dx \right]. \quad (51.b)$$

If a load resistor Z is connected between the electrodes, the voltage across Z is

$$SZ \frac{d\sigma_U}{dt} + \frac{\sigma_U}{\pi} \left(\frac{1}{\epsilon_1} + \frac{1}{\epsilon_2} \right) \int_0^{x_1+x_2+z} f(x)dx - \frac{1}{\pi} \left[\frac{1}{\epsilon_1} \int_{x_1}^{x_1+z} f(x)dx + \frac{1}{\epsilon_2} \int_{x_2}^{x_2+z} f(x)dx \right] = 0. \quad (52)$$

This is a first-order ODE from which the output charge density $\sigma_u(t)$ can be determined.

From Eq. (52), the current, voltage, and power against various resistances can be calculated numerically. Figure 11(e) shows the peak current, voltage, and power output predicted by the DDEF model. It is observed that the peak voltage is lower at lower resistances, leading to a small power output. When the resistance increases, the peak voltage increases; however, the peak current decreases significantly, and a low power results. Hence, the maximum peak power is obtained at an intermediate resistance. Therefore, three working regions are contained in the output behavior, as can be experimentally verified. Figure 11(f) shows good agreement between simulated and experimental peak power values.

A comparison of the experimental V_{OC} vs the separation distance for the DDEF model and the CA model is illustrated in Fig. 11(g). The V_{OC} predicted by the CA model increases proportional to the separation distance which deviates from the experimental results. However, simulations from the DDEF model show an increasing trend with the increase in the relative displacement and plateaus appear after a threshold separation. This trend is close to what is observed in experiments, a result which can be explained by the variation of the total electric field originating from the four charged layer. Therefore, the DDEF model is more accurate than the CA model in predicting the basic output performance of TENGs. Figures 11(h)–11(j) show the outputs from the planar TENG device and non-planar device based on the DDEF model. These results demonstrate that the output performance of the non-planar TENG device can be accurately predicted by the method of DDEF modeling, demonstrating the model's ability to simulate TENGs with different geometries and complexities.

Another type of CS mode TENG is shown in Fig. 12(a) composed by one dielectric layer and two metal sheets. It is noticed that the top sheet not only functions as electrode but also as the triboelectric layer. Thus, both tribocharges and induced charges are distributed in the top sheet. When it moves up and down, albeit the tribocharges are static on the metal surface, the induced charges vary due to the potential difference between the two electrodes, resulting in a variation of residual charges on the top electrode. The overall electric field acting on the electrodes also changes with the separation distance.^{4,46–48} According to Eq. (48), the electric potentials at the top electrode (ϕ_1) and attached electrode (ϕ_2) are

$$\phi_1 = -\frac{\sigma_U}{\pi\epsilon_0} \int_0^{x_1+z(t)} f(x)dx + \frac{\sigma_T}{\pi\epsilon_0} \int_0^{z(t)} f(x)dx, \quad (53.a)$$

$$\phi_2 = \frac{\sigma_U}{\pi\epsilon_1} \int_0^{x_1+z(t)} f(x)dx - \frac{\sigma_T}{\pi\epsilon_1} \int_{x_1}^{z(t)+x_1} f(x)dx, \quad (53.b)$$

where x_1 and ϵ_1 are the thickness and dielectric constant of the dielectric layer, respectively. Based on Eq. (7), the voltage across a load resistor Z is obtained from the time-dependent differential equation

$$LWZ \frac{d\sigma_U}{dt} + \frac{\sigma_U}{\pi} \left(\frac{1}{\epsilon_0} + \frac{1}{\epsilon_1} \right) \int_0^{x_1+z(t)} f(x)dx - \frac{\sigma_T}{\pi} \left[\frac{1}{\epsilon_1} \int_{x_1}^{x_1+z(t)} f(x)dx + \frac{1}{\epsilon_0} \int_0^{z(t)} f(x)dx \right] = 0. \quad (54)$$

2. Electrical potential of the SEC mode TENG

For the SEC mode TENG [Fig. 11(e)], using the method of DDEF modeling and Eq. (48), the potentials of the primary

electrode (node 2) and reference electrode (node 3) are given by⁴⁷

$$\phi_1 = -\frac{\sigma_U}{\pi\epsilon_0} \int_0^d f(x)dx + \frac{\sigma_T}{\pi\epsilon_0} \int_0^{z(t)} f(x)dx, \quad (55.a)$$

$$\phi_2 = \frac{\sigma_U}{\pi\epsilon_0} \int_0^d f(x)dx - \frac{\sigma_T}{\pi\epsilon_0} \int_d^{z(t)+d} f(x)dx, \quad (55.b)$$

where d is the separation distance between the primary electrode and the reference electrode. Based on Eq. (7), the governing equation of the SEC mode TENG is derived by

$$LWZ \frac{d\sigma_U}{dt} + \frac{2\sigma_U}{\pi\epsilon_0} \int_0^d f(x)dx + \frac{\sigma_T}{\pi\epsilon_0} \left[\int_d^{d+z(t)} f(x)dx - \int_0^{z(t)} f(x)dx \right] = 0, \quad (56)$$

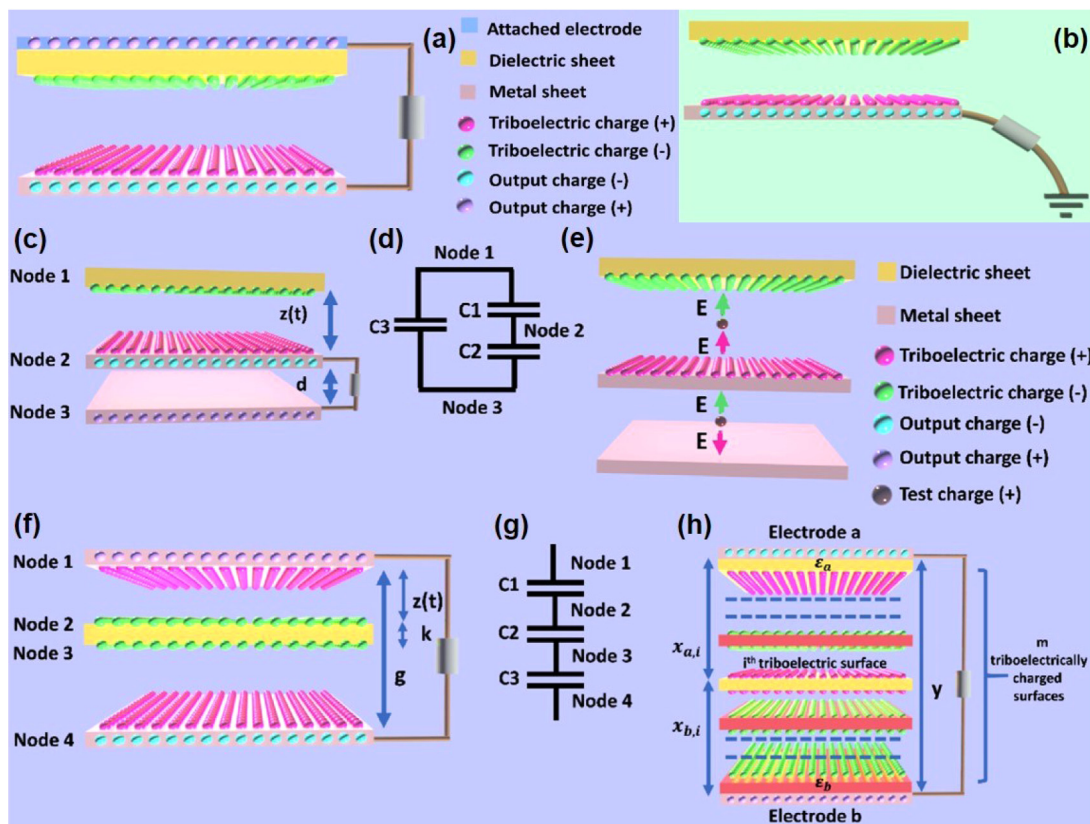


FIG. 12. (a) Schematic illustration of a metal-dielectric vertical contact-separation mode TENG; (b) schematic illustration of a single-electrode mode TENG with a grounded primary electrode through an output load; (c) schematic illustration, and (d) corresponding equivalent circuit model of a typical single-electrode mode TENG; (e) the overall electric field behavior of the single-electrode mode TENG when the triboelectric layers are separated by an air gap; (f) schematic illustration, and (g) corresponding equivalent circuit model of a contact free-standing mode TENG; (h) schematic illustration of a TENG with m triboelectrically charged surfaces.⁴⁸ Reproduced with permission from Dharmasena *et al.*, *Nano Energy* **48**, 391 (2018). Copyright 2018 Elsevier.

where Z is the external load resistance across the two electrodes. Note that this equation is a first-order ODE, from which the output charge density $\sigma_u(t)$ can be solved,

$$LWZ \frac{d\sigma_U}{dt} + \frac{2\sigma_U}{\pi\epsilon_0} \int_0^\infty f(x)dx - \frac{\sigma_T}{\pi\epsilon_0} \int_0^{z(t)} f(x)dx = 0. \quad (57)$$

The primary electrode can be connected to ground directly [Fig. 12(b)]. As seen in Fig. 12(b), when the dielectric layer moves up and down, the total electric field acting on the primary electrode changes. Thus, the electric potential of the primary electrode increases/decreases, leading to charge transfer between ground and the electrode. Based on Eq. (48), the electric potential of the primary electrode is

$$\phi_1 = -\frac{\sigma_U}{\pi\epsilon_0} \int_0^\infty f(x)dx + \frac{\sigma_T}{\pi\epsilon_0} \int_0^{z(t)} f(x)dx. \quad (58)$$

And the voltage across the connected resistor Z can be obtained by solving the time-dependent differential equation,

$$LWZ \frac{d\sigma_U}{dt} + \frac{\sigma_U}{\pi\epsilon_0} \int_0^\infty f(x)dx - \frac{\sigma_T}{\pi\epsilon_0} \int_0^{z(t)} f(x)dx = 0. \quad (59)$$

$$LWZ \frac{d\sigma_U}{dt} + \frac{2\sigma_U}{\pi\epsilon_0} \int_0^g f(x)dx + \frac{\sigma_T}{\pi\epsilon_0} \left[\int_0^{z(t)} f(x)dx - \int_{k+z(t)}^g f(x)dx - \int_0^{g-z(t)-k} f(x)dx + \int_{g-z(t)}^g f(x)dx \right] = 0. \quad (61)$$

Note that this equation is a time-dependent differential equation that can be solved for the charge density $[\sigma_u(t)]$.

In brief, based on the method of DDEF modeling, theoretical models for several types of TENGs have been developed including the non-planar TENG device. It has been demonstrated that the method of DDEF modeling and 3D mathematical modeling, which are established based on the quasi-electrostatic model, are more accurate than the CA model in predicting the basic outputs of TENGs. On the other hand, the DDEF model is just one special case of the time-dependent 3D mathematical model, for which the movable part of the TENG moves in a designed direction, for example, the vertical direction. We note that predicting the outputs of a TENG device moving in a horizontal direction has never been reported based the DDEF model.

IV. EQUIVALENT ELECTRICAL CIRCUIT MODELS OF TENGs

A. Capacitive model of TENGs

Using a first-order lumped-parameter equivalent circuit model, a TENG device is represented by a serial connection of an

3. Electrical potential of the contact-mode freestanding mode TENGs (FSTENGs)

Consider a dielectric contact-mode FSTENG geometry illustrated in Fig. 12(f). With the dielectric layer moving up and down, tribocharges are generated between nodes 1 and 2 and nodes 3 and 4, respectively. Since the electric fields originating from these nodes lead to an electric field acting on the bottom electrode, the electric potential of node 4 strongly depends on the variation of these electric fields. For the same reason, the electric potential at the top electrode (node 1) is also affected by changes in the total electric field generated from the charged layers. Using Eqs. (11) and (48), the electric potentials of the nodes 4 (ϕ_1) and 1 (ϕ_2) are⁴⁷

$$\phi_1 = -\frac{\sigma_U}{\pi\epsilon_0} \int_0^g f(x)dx + \frac{\sigma_T}{\pi\epsilon_0} \int_0^{g-z(t)-k} f(x)dx - \frac{\sigma_T}{\pi\epsilon_0} \int_{g-z(t)}^g f(x)dx, \quad (60.a)$$

$$\phi_2 = \frac{\sigma_U}{\pi\epsilon_0} \int_0^g f(x)dx + \frac{\sigma_T}{\pi\epsilon_0} \int_0^{z(t)} f(x)dx - \frac{\sigma_T}{\pi\epsilon_0} \int_{k+z(t)}^g f(x)dx. \quad (60.b)$$

When a load resistor Z is connected between the two electrodes, the potential difference will drive charges to flow from one electrode to the other. Kirchhoff's law states

ideal voltage source (V_{OC}) and the inherent capacitance (C_t) of TENG [Fig. 13(a)].^{40,41,53-57} The V_{OC} is generated by the potential difference between the two electrodes when there is no charge transferred. The inherent capacitance of a TENG always includes two parts [take the CS mode TENG as an example, Fig. 6(c)]: the C_{device} and C_{air} are connected in series, i.e., $1/C_t = 1/C_{device} + 1/C_{air}$. The capacitance C_{device} remains constant over time and includes the contribution from the dielectric layer and any additional capacitances connected in series to the dielectric layer. The C_{air} is defined as the air gap contribution which changes over time. This equivalent circuit model is the capacitive model which is proposed based on the lumped parameter circuit theory.^{1,41,45}

Furthermore, a non-ideal factor that affects the ideal outputs of TENGs is the parasitic capacitance, which cannot be neglected and always exists in an electric circuit. As stated above, the essence of the TENG energy harvester is to employ a quasi-electrostatic system, any parasitic capacitance generated from the interruption of the electric field close to the TENG system will affect its output. The magnitude of the parasitic capacitance is usually comparable

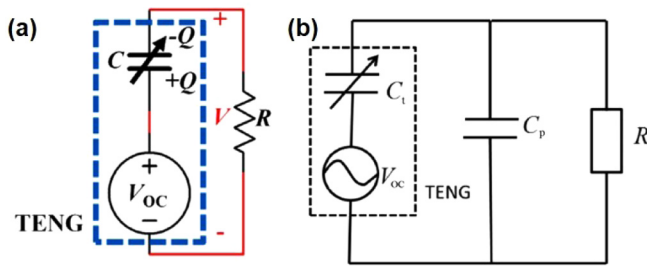


FIG. 13. (a) First-order lumped-parameter equivalent-circuit model for TENGs within the framework of the lumped circuit abstraction.⁴¹ Reproduced with permission from Niu *et al.*, *Nano Energy* **8**, 150 (2014). Copyright 2014 Elsevier. (b) Equivalent-circuit model for TENGs with the consideration of parasitic capacitance. The modeling proposed compromises circuit effects that cannot be ignored and significantly affect circuit performance in reality.⁴³ Reproduced with permission from Dai *et al.*, *Nano Res.* **10**, 157 (2017). Copyright 2018 Springer.

to a TENG's inherent capacitance, making the TENG sensitive to the external capacitance. The leakage mechanism is modeled via an additional parasitic capacitor in parallel to the C_{device} .^{43,58} The equivalent circuit model of the TENG including the additional parasitic capacitor is shown in Fig. 13(b). The capacitive model is the first theoretical model built for TENGs. Although there are limitations in this model, it provides a relatively simple way to understand the working principles of TENGs easily and conveniently.

1. Open-circuit voltage and short circuit current of TENGs

Take the CS mode TENG shown in Fig. 6(c) as an example. At OC conditions, there is no charge transferred between the two electrodes. The voltage at OC conditions is⁵⁴

$$V_{OC} = \frac{\sigma_T z(t)}{\epsilon_0}. \quad (62)$$

The output charge at SC conditions is given by

$$Q_{SC} = \frac{S\sigma_T z(t)}{d_0 + z(t)}, \quad (63)$$

where d_0 is the effective thickness of the dielectric layer, defined by $d_1/\epsilon_1 + d_2/\epsilon_2$. Then, the short-circuit current (I_{SC}) is derived by the differential computing of the Q_{SC} ,

$$I_{SC} = \frac{dQ_{SC}}{dt} = \frac{\sigma_T d_0 S}{(d_0 + z(t))^2} \frac{dz}{dt} = \frac{\sigma_T d_0 S v(t)}{(d_0 + z(t))^2}. \quad (64)$$

The V_{OC} -time and Q_{SC} -time relationships simulated from the CA model at small separation distances are similar to those of from the method of 3D mathematical modeling, as seen in Fig. 7.

2. Inherent capacitive behavior of TENGs

According to the traditional definition of capacitance, the capacitance of a TENG transducer is defined by

$$C = \frac{\epsilon_0 S}{d_0 + z(t)}. \quad (65)$$

Figure 14(b) shows a time-dependent capacitance of the CS mode TENG, and the corresponding air gap-time relationship is illustrated in Fig. 14(a). Here, the edge effect is ignored because the size of the TENG is much larger than the air gap and the thickness of the dielectric layer in this geometry.^{54,59} In general, the maximum capacitance C_{max} , minimum capacitance C_{min} , and their ratio ($C_{\text{max}}/C_{\text{min}}$) have significant influence on the energy conversion efficiency of the TENG system. C_{max} can be obtained when there is no relative movement; on the contrary, when the moving part reaches the largest distance, C_{min} is reached.

3. Governing equation of TENGs from the CA model

According to the CA model and the relationship between voltage, charge, and separation distance ($V-Q-x$), the governing equation of the CA model is given by^{40,41,54}

$$V = -\frac{Q}{C(x)} + V_{OC}(x), \quad (66)$$

where $C(x)$ represents the capacitance of the TENG, Q is the output charge, and V_{OC} is the open-circuit voltage.

When an external load resistor Z is connected between the electrodes, combining Ohm's law and Kirchhoff's laws leads to the governing equation for the CS mode TENG [Fig. 6(c)],

$$Z \frac{dQ}{dt} = -\frac{Q}{S\epsilon_0} (d_0 + z(t)) + \frac{\sigma_T z(t)}{\epsilon_0}. \quad (67)$$

Note that this is a first-order ODE, in which the output charge is taken as the dependent variable. With the boundary condition $Q(t=0) = 0$, this equation can be solved to give

$$Q(t) = \frac{1}{Z} \exp\left[-\frac{1}{Z} \int_0^t \frac{dt'}{C(z(t'))}\right] \times \int_0^t V_{OC}(z(t')) \exp\left[\frac{1}{Z} \int_0^{t'} \frac{dt''}{C(z(t''))}\right] dt'. \quad (68)$$

The current and voltage across the external load Z are given by

$$I(t) = \frac{V_{OC}}{Z} - \frac{1}{Z^2 C} \exp\left[-\frac{1}{Z} \int_0^t \frac{dt'}{C(z(t'))}\right] \times \int_0^t V_{OC}(z(t')) \exp\left[\frac{1}{Z} \int_0^{t'} \frac{dt''}{C(z(t''))}\right] dt', \quad (69)$$

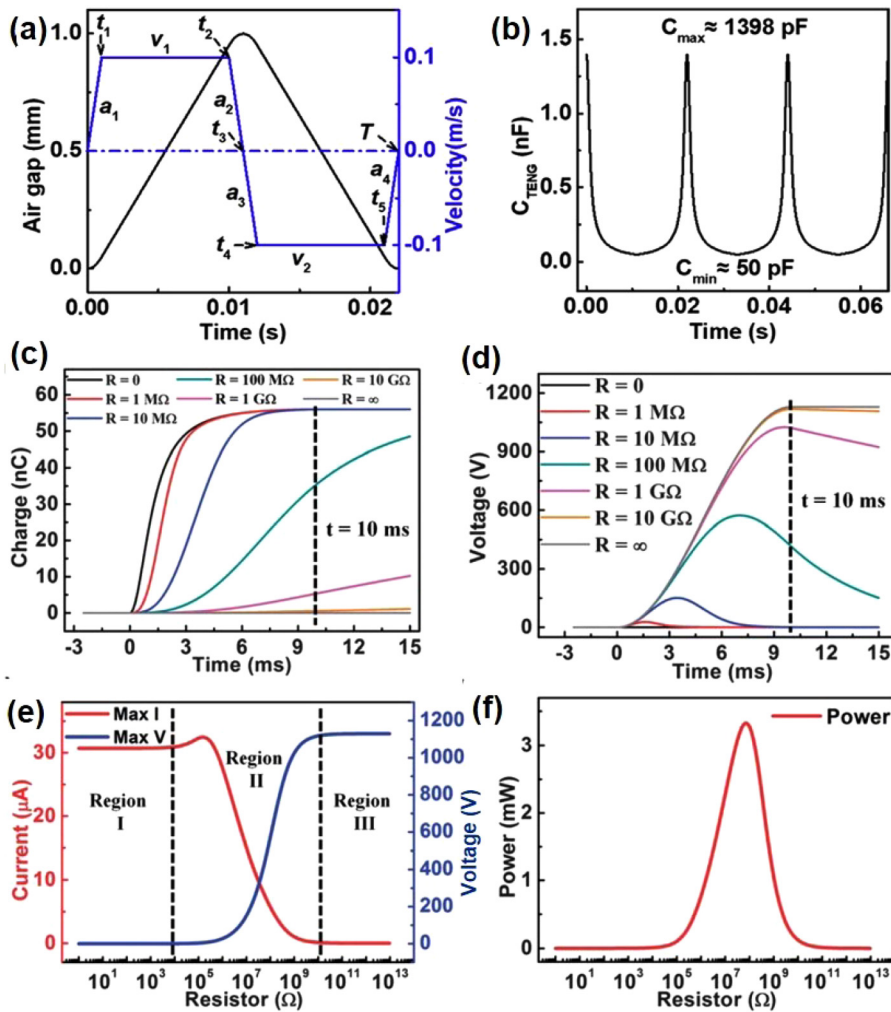


FIG. 14. Output performances of the vertical contact-separation mode TENG numerically calculated from the capacitive mode. (a) The time-dependent air gap, velocity (v), acceleration/deceleration (a), and (b) the corresponding total capacitance of the TENG.⁵⁹ Reproduced with permission from Zhang *et al.*, *Nano Energy*, **63**, 103856 (2019). Copyright 2019 Elsevier. Time-dependent (c) output charge, and (d) voltage at different load resistances of the TENG; (e) the three-working regions, and (f) the peak power behavior of the TENG.⁵⁴ Reproduced with permission from Niu *et al.*, *Energy Environ. Sci.* **6**, 3576 (2013). Copyright 2013 Royal Society of Chemistry.

$$V(t) = V_{OC} - \frac{1}{ZC} \exp\left[-\frac{1}{Z} \int_0^t \frac{dt'}{C(z(t'))}\right] \times \int_0^t V_{OC}(z(t')) \exp\left[\frac{1}{Z} \int_0^{t'} \frac{dt''}{C(z(t''))}\right] dt'. \quad (70)$$

The numerical calculations for the first half-cycle movement are plotted in Figs. 14(c)–14(f). It is apparent that there are three working regions in Fig. 14(e), which is similar to the behavior of the DDEF model [Fig. 11(e)]. In the transition region, where the maximum current drops dramatically but the maximum voltage increases, the peak power is obtained. The corresponding load resistance is denoted the “optimum resistance.” In fact, this “optimum resistance” is only relevant for the first half cycle, since the TENG is still in the transient stage. For this “optimum resistance” in transient conditions one does not, however, obtain the largest average power to steady state.

The same method can be utilized to explore the LS mode TENG. As shown in Fig. 6(e), using Eq. (7), the governing equation of the LS mode TENG is written as⁵¹

$$V = -\frac{d_0}{w\epsilon_0(l-a(t))}Q + \frac{\sigma_T d_0 a(t)}{\epsilon_0(l-a(t))}, \quad (71)$$

where w and l are the length and width of the dielectric layer, respectively. With the initial condition $Q(t=0)=0$, the output charge Q is solved as

$$Q(t) = \sigma_T S \left[1 - \exp\left(\frac{d_0}{\epsilon_0 Z S} \int_0^t \frac{l}{l-a(t')} dt'\right) \right] - \frac{\sigma_T d_0}{\epsilon_0 Z} \int_0^t \exp\left(\frac{d_0}{\epsilon_0 Z S} \int_t^{t'} \frac{l}{l-a(t'')} dt''\right) dt', \quad (72)$$

where $S = wl$ represents the surface area of the dielectric layer. The output voltage is given by

$$V = \frac{\sigma_T d_0}{\epsilon_0} \left[\frac{l}{l - a(t')} \exp\left(-\frac{d_0}{\epsilon_0 ZS} \int_0^t \frac{l}{l - a(t')} dt'\right) + \frac{d_0}{\epsilon_0 ZS} \frac{l}{l - a(t')} \int_0^t \exp\left(\frac{d_0}{\epsilon_0 ZS} \int_t^{t'} \frac{l}{l - a(t'')} dt''\right) dt' - 1 \right]. \quad (73)$$

Therefore, the capacitance of the LS mode TENG can be calculated in a standard way: as the ratio between the output charge and voltage across the TENG.

On the other hand, similar to a traditional ZC circuit, the transient period from the relaxation state to steady state depends on the time constant τ given by the product ZC. For a TENG device, due to its time-varying capacitance, the relaxation time (τ_{relax}) is closely related to the effective capacitance [or root mean square value of the $C(t)$]. As stated above, the capacitance of a TENG is composed of two parts: the fixed capacitance introduced from the dielectric film and the time-varying capacitance due to the relative movement. The fixed capacitance (C_{in}) represents the dc component or the average value of $C(t)$, while the time-varying capacitance is a function of time, its effective value $C_{\text{ac}}(C_{\text{ac,rms}})$ is derived from⁴⁶

$$C_{\text{ac(rms)}} = \sqrt{\frac{1}{T} \int_0^T [C_{\text{ac}}(t)]^2 dt}. \quad (74)$$

Then, the effective of $C(t)$ is defined by

$$C_{\text{rms}} = \sqrt{C_{\text{in}}^2 + (C_{\text{ac(rms)}})^2}. \quad (75)$$

Note that in a dc network, the current/voltage of a capacitive circuit approaches zero after approximately five time constants. This result is equally applicable to a TENG circuit. Therefore, the relaxation time of the TENG circuit is

$$\tau_{\text{relax}} = 5ZC_{\text{rms}}. \quad (76)$$

And the corresponding minimum number of cycle k_{relax} is

$$k_{\text{relax}} = \frac{\tau_{\text{relax}}}{T}, \quad (77)$$

indicating that after k_{relax} cycles, the TENG device reaches steady state.

The CA model is proposed based on the capacitive characteristics of TENGs, through which the V - Q - x relationships, inherent capacitance, and basic outputs of TENGs can be clearly demonstrated. Moreover, the CA model is also available to other harvesting systems such as the electrostatic harvester. The theoretical model of the electrostatic harvester is similar to that of the TENG, except for the fact that the contacting surface charges of TENGs are created by CE. In addition, using the CA model, the internal impedance and the relaxation time of TENGs can be easily understood. As the CA model is built based on infinite charged planes, the accuracy of predictions made by this model stays within a certain range of applicability. Outside this range, deviations from experimental results occur, especially at a larger relative movement of TENGs.^{4,47} This is mainly due to the lack of finite-edge effects in this model.

B. Norton's equivalent circuit model

In general, a simple resistive circuit can be analyzed using Kirchhoff's laws in combination with Ohm's law. However, to simplify a complex circuit structure, Thevenin and Norton equivalent circuits are usually considered. For instance, a Norton equivalent circuit consists of an independent current source in parallel with the Norton equivalent resistance. The Norton current equals the short-circuit current at the terminal of interest, and the Norton resistance is identical to the Thevenin resistance. Through the equivalent of Norton's theorem for a linear-two-terminal system, a TENG can be represented by a time-variant source [$I_S(t)$] in parallel with the TENG internal impedance [$Z_S(t)$] [Fig. 15(b)].⁶⁰

Take a TENG with m triboelectrically charged surfaces as an example [Fig. 12(h)], when an external load (Z_L) is connected between the two electrodes, the governing equation derived from the method of DDEF modeling is given by⁶⁰

$$LWZ_L \frac{d\sigma_U}{dt} + \frac{\sigma_U}{\pi} \left(\frac{1}{\epsilon_a} + \frac{1}{\epsilon_b} \right) \int_0^y f(x) dx - \frac{1}{\pi} \left[\sum_{i=1}^m \left(\frac{\sigma_{T,i}}{\epsilon_a} \int_{x_{a,i}}^{\infty} f(x) dx - \frac{\sigma_{T,i}}{\epsilon_b} \int_{x_{b,i}}^{\infty} f(x) dx \right) \right] = 0, \quad (78)$$

where $\sigma_U(t)$ is the output charge density, $\sigma_{T,i}$ is the tribocharge density of the i th tribo-charged surface, ϵ_a and ϵ_b are dielectric constants, $x_{a,i}$ and $x_{b,i}$ are distances from the i th charged surface to respective electrodes. y is the separation distance between the two electrodes. This equation is a time-dependent differential equation; and solving it, the output charge density can be evaluated.

As previously described, the capacitance of a typical CS mode TENG is described by Eq. (65). For this multilayer CS mode TENG, its effective capacitance $K(t)_{\text{eff}}$ is defined by

$$K(t)_{\text{eff}} = \frac{LW}{G(t)} = \left[\frac{1}{LW\pi} \left(\frac{1}{\epsilon_a} + \frac{1}{\epsilon_b} \right) \int_0^y f(x) dx \right]^{-1}, \quad (79)$$

where the $G(t)$ is

$$G(t) = \frac{1}{\pi} \left(\frac{1}{\epsilon_a} + \frac{1}{\epsilon_b} \right) \int_0^y f(x) dx. \quad (80)$$

Through $K(t)_{\text{eff}}$, the impedance behavior of this TENG can be explored. For instance, at a given time t , and with a relatively low frequency n ($n < 1000$ Hz), the internal impedance of the [$Z_S(t)$] is

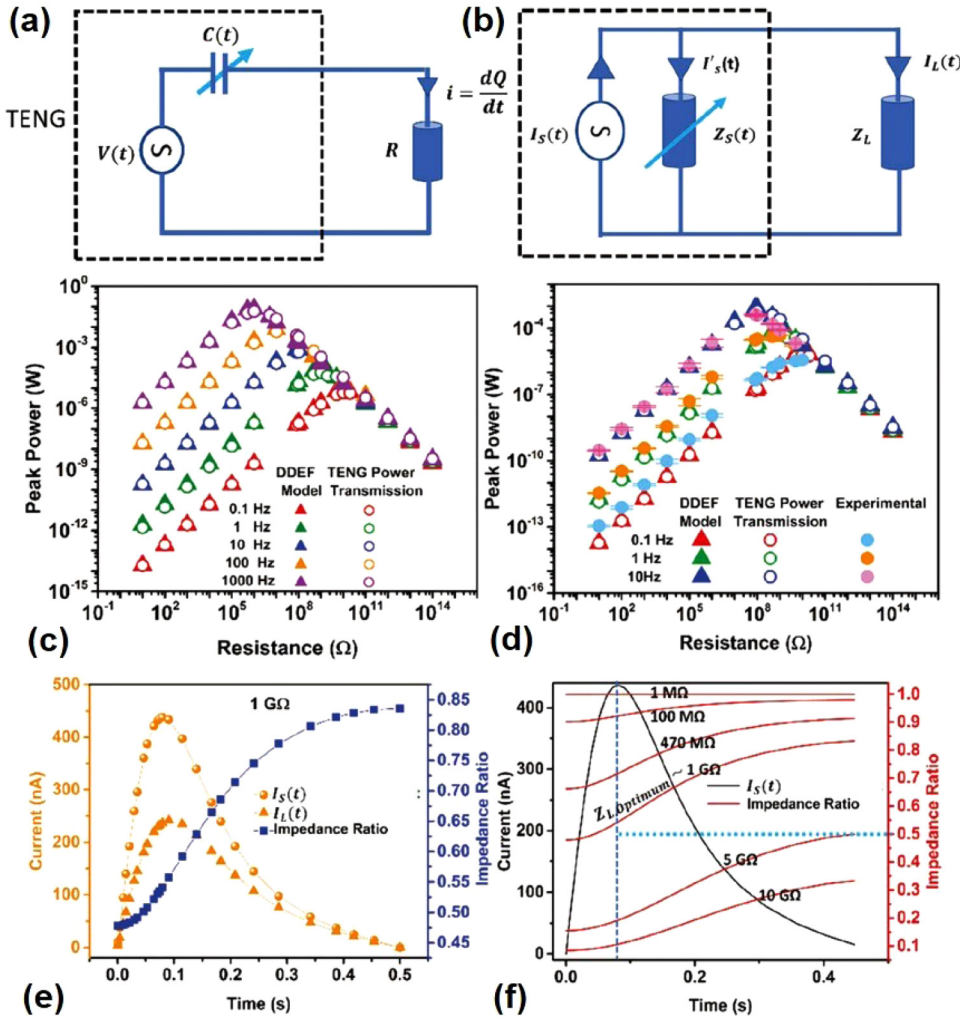


FIG. 15. Norton's equivalent circuit model and the output characteristics for a vertical contact-separation mode TENG. (a) Conventional equivalent circuit mode of TENGs; (b) the corresponding Norton's equivalent circuit mode, from which the TENG is represented with a time-varying current source $[I_S(t)]$ in parallel with TENG impedance $[Z_S(t)]$; (c) a comparison of peak power between the Distance-Dependent Electric Field mode and Norton's circuit model at different working frequencies; (d) experimental peak power compared with the corresponding calculations under different frequencies; (e) time-dependent current source $[I_S(t)]$, current through the external load $[I_L(t)]$, and impedance ratio under (e) $Z_L = 1G\Omega$ for the TENG, and (f) different external load resistances for the TENGs.⁶⁰ Reproduced with permission from Dharmasena *et al.*, *Adv. Energy Mat.* 8, 1802190, (2018). Copyright 2018 Wiley.

derived by

$$Z_S(t) = \frac{1}{2\pi n K(t)_{\text{eff}}} = \frac{1}{2\pi^2 L W n} \left(\frac{1}{\epsilon_a} + \frac{1}{\epsilon_b} \right) \int_0^y f(x) dx. \quad (81)$$

Note that this equation is essentially equal to Eq. (41), and both of them are functions of the TENG structures and mechanical frequency.

As shown in Fig. 15(b), when an external load (Z_L) is connected in parallel with $I_S(t)$ and $Z_S(t)$, the current generated by the TENG will be split and flow through $Z_S(t)$ and Z_L . Therefore,

$$I_L(t) = I_S(t) \frac{Z_S(t)}{Z_S(t) + Z_L}, \quad (82)$$

where $I_L(t)$ stands for the current flow Z_L . This equation is also denoted as the power transfer equation of TENGs. Additionally,

the output power $[P_{\text{out}}(t)]$ is estimated by

$$P_{\text{out}}(t) = I_L(t)^2 Z_L. \quad (83)$$

It should be noticed that the current $[I_L(t)]$ through Z_L mainly depends on the short-circuit current and the impedance ratio described by $(Z_S(t))/(Z_S(t) + Z_L)$. According to Norton's equivalent circuit, the current source $I_S(t)$ can be represented by the short-circuit current of the TENG. The current source $I_S(t)$ is given by

$$I_S(t) = I_{\text{SC}}(t) = LW \frac{d}{dt} \frac{\sigma_T \left[\frac{1}{\epsilon_1} \int_{x_1}^{x_1+x(t)} f(x) dx - \frac{1}{\epsilon_2} \int_{x_2}^{x_2+x(t)} f(x) dx \right]}{\left(\frac{1}{\epsilon_1} + \frac{1}{\epsilon_2} \right) \int_0^{x_1+x_2+x(t)} f(x) dx}. \quad (84)$$

The numerical calculations based on above equations and the experimental results are demonstrated in Fig. 15. From Figs. 15(c) and 15(d), it is found that the experimental results are in agreement with the theoretical predications from both the DDEF model and Norton's equivalent circuit model. The impedance plots shown in Figs. 15(e) and 15(f) illustrate that changing the external load (Z_L) causes the i -ratio to vary, and the related output current [$I_S(t)$] changes accordingly. The overall global peak power occurs at around $Z_L = 1 \text{ G}\Omega$, at which the i -ratio ideally coincides with the peak [$I_S(t)$]. The above results provide a visualization method for a TENG to map the occurrence of overall global peak power even at different structural and mechanical motions.

In general, the maximum power transfer theorem reveals that the maximum power transferred from the energy source to the external load takes place when the impedance of the load is equal to the impedance of the energy source. For the TENGs, the power transfer equation suggests that this will happen when the i -ratio is close to 0.5, which means the Z_L should be close to $Z_S(t)$. This is why we find the corresponding TENG impedance plots shown in Fig. 15(f). The conventional circuit model of TENG is modeled by a voltage source in series with a variable capacitor, which does not include the resistor. Through Thevenin's equivalent circuit, the time-varying capacitor is replaced by a corresponding TENG impedance [$Z_S(t)$]; and the related voltage source is then regarded as the Voc of the TENG [Fig. 15(b)]. Next, the voltage source is replaced by a current source being equal to the short circuit current [$I_S(t)$] of the TENG device, and the impedance element does not change while its network changes from the series connection owing to Norton's equivalent circuit model. In other words, due to the lumped parameter circuit theory, a TENG is finally regarded as a current source in parallel with the TENG impedance, both of which are time-varying variables. However, by comparing simulated results based on the above equations and experimental results, deviations are found (Fig. 15). Due to the limited space and time, this deviation will not be discussed further in this review. Note that the work published in *Applied Physics Reviews* (Ref. 46) address this phenomenon.

C. Methods of dimensional analysis and FEM simulation of TENGs

1. Dimensional analysis and optimization principles of TENGs

Dimensional analysis often gives additional physics insight. The motivation behind dimensional analysis is that any dimensional equation can be written in an entirely equivalent non-dimensional form. It is important to note that the output performance of a TENG is governed in a complicated way by a set of many parameters. Every single parameter is interlinked with the other parameters in the modeling dynamics, and an unexpected change in any of them will disrupt an optimal strategy; thus a new specific condition for the best output should be analyzed again.^{58,61-63} Therefore, considering a multi-parameter analysis is necessary, and this is conveniently done using dimensional analysis.^{46,58,62,63}

To convert the governing equation of TENGs to a dimensionless form, several reduced parameters must be defined first. From

the 3D mathematical model of the LS mode TENG, the corresponding governing equation of Eq. (40) becomes⁴⁶

$$-Z^* \frac{dQ_U^*}{dt^*} = \phi_1^* - \phi_2^*, \quad (85)$$

where $Q_U^* \equiv \frac{Q_U}{bL\rho_T}$, $Z^* \equiv \frac{(L-a_{\max})Zb\epsilon_0}{d_0}$, $t^* = \phi = \omega t$, $\phi_1^* \equiv \frac{\phi_1(x, y, z)}{F(\Pi)}$, $\phi_2^* \equiv \frac{\phi_2(x, y, z)}{F(\Pi)}$, and $F(\Pi) = \frac{\sigma_T L d_0}{(L-a_{\max})\epsilon_0}$. Equation (85) is a dimensionless form of the governing equation for the LS mode TENGs, which is also available to any other TENGs with different configurations and structures. With the initial condition $Q_U^*(\varphi) = 0 = 0$, the analytical solution of Q_U^* is given by

$$Q_U^*(\varphi) = \frac{1}{Z^*} \int_0^\varphi [\phi_2^*(\varepsilon) - \phi_1^*(\varepsilon)] d\varepsilon. \quad (86)$$

Then, the dimensionless current (I^*), power (P^*), average power (P_{ave}^*), and electrical energy (E^*) delivered to the external resistor (Z^*) can be derived. Moreover, the effective dimensionless output charges ($Q_{u,rms}^*$), current (I_{rms}^*), voltage (V_{rms}^*), power (P_{rms}^*), electric energy (E_{rms}^*) are also obtained. Furthermore, the physical parameters such as the electric displacement (D^*), displacement current (I_D^*) can be evaluated.

Figure 16 illustrates the dimensionless analysis of the alternating current outputs of the LS mode TENG according to the method of 3D mathematical modeling. Interestingly, the Q^*V^* plots from the first cycle is not closed, meaning that the operation of the LS mode TENG still works in a transition state. This phenomenon is applied to other types of TENGs with different geometries. If the TENGs are operated in a steady state, the Q^*-V^* plots will be closed, as demonstrated in Fig. 15(b). When the optimum resistance is loaded, the corresponding area of Q^*-V^* plot changes to the biggest when compared with that of from other different external loads. In this way, the largest dimensionless power and energy [Fig. 15(c)] can be predicted.

The structural figure-of-merits (FOMs) have been defined and proposed to explore the relationship between the structure and outputs of a TENG.^{32,55} The figure-of-merits: FOM_T , FOM_{RS} , and FOM_S are shown in Fig. 15(d), where FOM_T represents the TENG operated in the steady state; FOM_{RS} and FOM_S represent the structural FOM of TENGs for Z_{opt} and infinite resistor, refer to Shao *et al.* (Ref. 55) and Zi *et al.* (Ref. 32), respectively. It is seen that the FOM_T is smaller than the FOM_{RS} and FOM_S , this is because the latter two are calculated from ideal conditions that all charges are transferred in one cycle; while the FOM_T represent the output when only part of the charges flow between the two electrodes of TENGs.

In a similar way, the governing equation of Eq. (66) from the CA model is converted to the dimensionless form⁵⁸

$$Z^* \frac{dQ^*}{dt^*} + Q^* \left(\frac{1}{C^*} + z^* \right) = z^*, \quad (87)$$

where $Z^* \equiv \omega Z_L C_{air} = \frac{Z_L A \omega \epsilon_0}{z_{\max}}$, $C^* \equiv \frac{C_{device}}{C_{air}}$, $z^* \equiv \frac{z(t)}{z_{\max}}$, $Q^* \equiv \frac{Q}{S\sigma_T}$. With the initial condition of $Q^*(0) = 0$, the analytical solution is obtained by

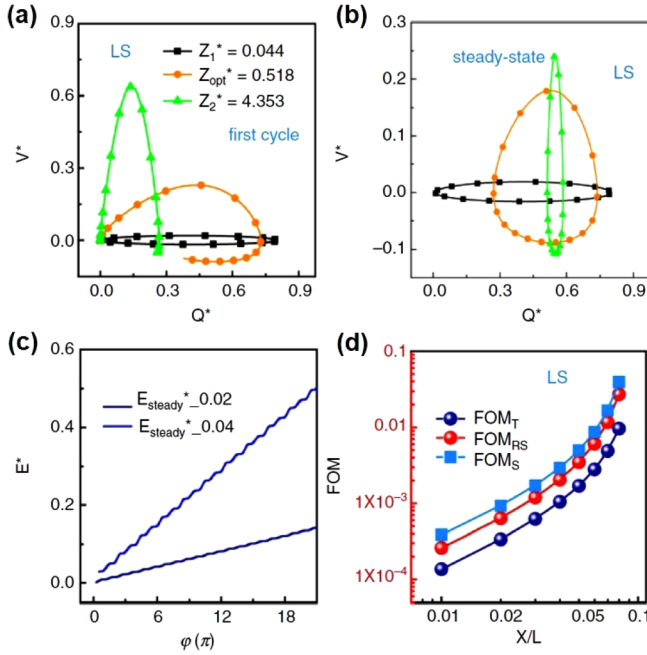


FIG. 16. Dimensionless analysis of the alternation current output performances for the lateral-sliding mode TENG calculated from the three-dimensional mathematical model. Plots of dimensionless voltage (V^*) and charge (Q^*) from the first cycle (a) to steady state cycle (b) under different dimensionless load resistance (Z^*); (c) comparison of dimensionless output energy (E^*) harvested in steady state for different x_{\max} ; (d) the figure-of-merits calculated in steady state (FOM_T) for the lateral-sliding mode TENG. Note that FOM_{RS} and FOM_S represent the structural figure-of-merits of TENGs for Z_{opt} and infinite resistor, refer to Shao *et al.* (Ref. 55) and Zi *et al.* (Ref. 32), respectively.⁴⁶ Reproduced with permission from Shao *et al.*, *Appl. Phys. Rev.* 7, 011405 (2020). Copyright 2020 AIP Publishing LLC.

the integral factor method,

$$Q^*(\theta) = \frac{\int_0^\theta (1 - \cos t) \cdot \exp\left[\frac{1}{2Z^*} \left(\frac{2t}{C^*} + t - \sin t\right)\right] dt}{2Z^* \exp\left[\frac{1}{2Z^*} \left(\frac{2\theta}{C^*} + \theta - \sin \theta\right)\right]}. \quad (88)$$

In steady state where $Q(\theta) = Q(\theta + 2\pi)$, the integral in Eq. (88) can be replaced with one that runs over one period,

$$\begin{aligned} \dot{Q}_{\text{steady}}(\theta) &= \frac{\exp\left(\frac{\sin \theta}{2Z^*}\right)}{2Z^* \left(\exp\left[\frac{\pi}{Z^*} \left(\frac{2}{C^*} + 1\right)\right] - 1\right)} \\ &\times \int_0^{2\pi} [1 - \cos(t + \theta)] \cdot \exp\left[\frac{1}{2Z^*} \left(\frac{2t}{C^*} + t - \sin(t + \theta)\right)\right] dt. \end{aligned} \quad (89)$$

Additionally, with the solved Q^* , the dimensionless current, voltage, and power can also be calculated. For instance, the average dimensionless power is characterized by

$$\overline{P^*} = \frac{1}{2\pi} \int_{\text{cycle}} I^{*2} Z^*. \quad (90)$$

Using this equation, the output power can be optimized with respect to Z^* and C^* . The maximum condition for the P^* is proved by

$$Z^* = 1.14, 1/C^* = 0.82, 2\pi\overline{P^*} = 0.127. \quad (91)$$

It is important to note that these equations define the optimum conditions to get the maximum average output power of TENGs based on the CA model.

Similar to the optimal conditions for the quasi-electrostatic model, this approach explains how different physical parameters must be optimized for the CA model. For instance, if two independent sets of physical parameters yield the same Z^* and C^* , they yield identical operation conditions. By using the dimensionless average power, the real power density is given by

$$\frac{\overline{P}}{S} = \overline{P^*} \cdot \frac{\sigma_T^2 \omega z_{\max}}{\epsilon_0}. \quad (92)$$

Setting P^* to its maximum value, a “device figure of merit” for power density in CS mode TENG is defined as

$$FOM_{\text{device}} = 0.064 \cdot \frac{\sigma_T^2 \overline{v}}{\epsilon_0}, \quad (93)$$

where $v = \omega z_{\max}/\pi$ is the average speed of the mechanical motion. It is seen that the FOM_{device} is a function of surface charge density (at the steady state) and average speed of the CS mode TENG.

Figure 17 illustrates the principle of optimization for power generation and dimensionless parameter analysis. From Figs. 17(a)–17(c), it is observed that the average power is optimized with a balance of both matching load resistance and current. At optimal conditions, the time-varying ZC product of the TENGs match the mechanical motion period during the cycle. For good matching, a large load resistance is required to compensate the large $1/C_{\text{device}}$, resulting in a low current and a small average power. On the contrary, with a small $1/C_{\text{device}}$, a high current is generated. This leads to a mismatch with the mechanical triggering, thus resulting in a small average power again. Similar trends for the dimensionless average power are found in Figs. 17(d)–17(e). Although the power during the transient behavior is higher than that in the steady state, the related external load does not correspond to optimum conditions. This is mainly because this type of matching will lead to smaller average power in steady state. Hence, it is demonstrated again that the optimum power and related resistance are available from steady state and not from the transient behavior of TENGs. The optimum resistance calculated from Eq. (42) or by making the product of ZC equal to the mechanical motion period specifies identical TENG device optimum conditions convenient to realize maximum average

power generation. Furthermore, it should be noticed that the optimum resistance of TENGs is only a function of its basic structure and the operating frequency of TENGs.

The governing equation of TENGs, either based on the method of 3D mathematical modeling or the CA model, can always be reduced to the dimensionless form. Then, a set of theoretical models in connection with normalized governing equations can be developed through which multi-physical, multi-structural, and multi-mechanical factors can be analyzed simultaneously, allowing us to determine the optimum conditions of TENGs for any specific conditions.

2. FEM simulation of TENGs

In previously published studies, simulations are carried out so as to obtain the open-circuit voltage and capacitance function in the $V-Q-x$ relationship.^{40,51,54} A more general approach can be carried out using the finite element method (FEM), e.g., COMSOL Multiphysics.^{64–71} The AC/DC module in the COMSOL physics

interface can be used to simulate the V_{OC} and Q_{SC} of the TENG. In fact, the AC/DC module includes stationary and dynamic electric and magnetic fields in two- and three-dimensional spaces together with the traditional circuit.^{72,73} The physics interfaces are utilized to formulate and solve the differential form of Maxwell's equations together with initial and boundary conditions. For the TENG device, the AC/DC module can also model the distributions of electric field, electric displacement, polarization, electrostatic force, and so on.

When modeling the TENG device, the OC boundary condition is that the free charge on the electrodes is 0, i.e., no charges are transferred between the two electrodes, while the electrode potentials are the same for SC condition. The TENG device is immersed in vacuum or subject to insulated conditions. The tribocharges are uniformly distributed on each dielectric interfaces such that the total sum of tribocharges in the system is zero to maintain charge equilibrium. As illustrated in Fig. 18, the variation of the electric field E , electric displacement D , polarization P , and electric potentials at different separation distances are simulated and the TENG parameters can be evaluated.

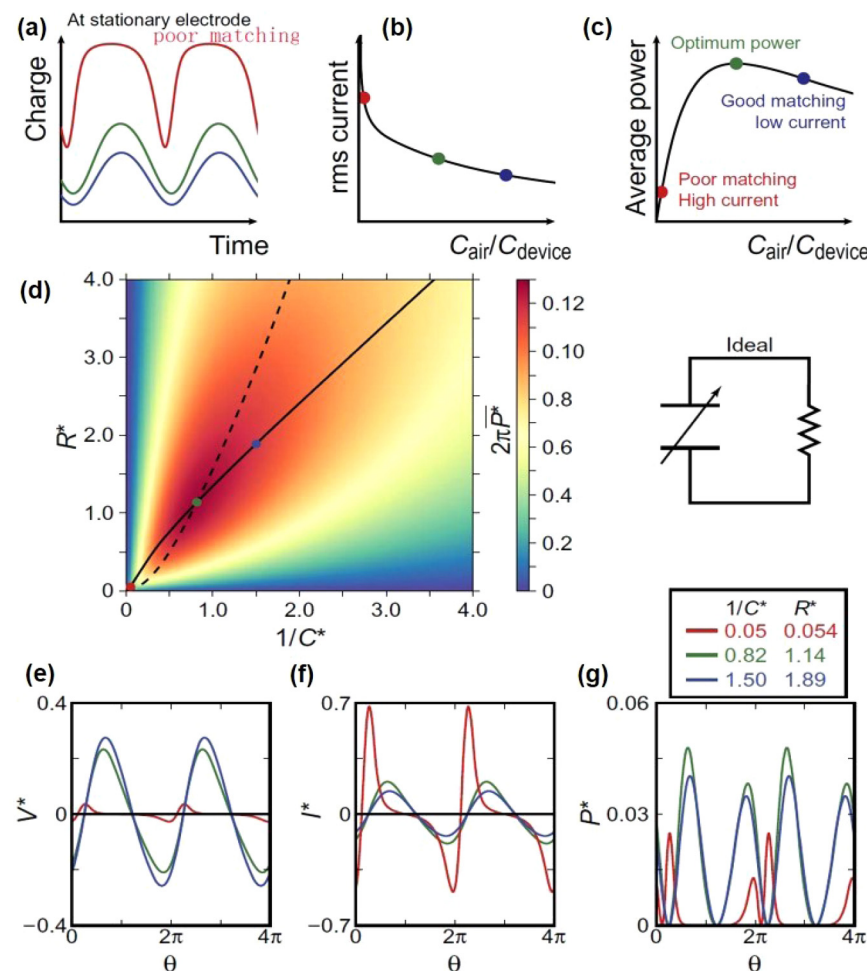


FIG. 17. Dimensionless analysis of the alternating current output performances for the vertical contact-separation mode TENG calculated from the capacitive mode. (a) The time-dependent voltage at different matching cases of the TENG; the influence of C_{air}/C_{device} on the (b) root-mean-square current, and (c) average power; (d) power map for the two dimensionless parameters R^* and $1/C^*$, and the color stands for the dimensionless power in each cycle $2\pi P^*$; phase-dependent of the dimensionless voltage (V^*), current (I^*), and power (P^*) at different matching cases in (e), (f), and (g), respectively.⁵⁸ Reproduced with permission from Peng *et al.*, *Sci. Adv.* 3, eaap8576 (2017). Copyright 2017 Science Publishing Group.

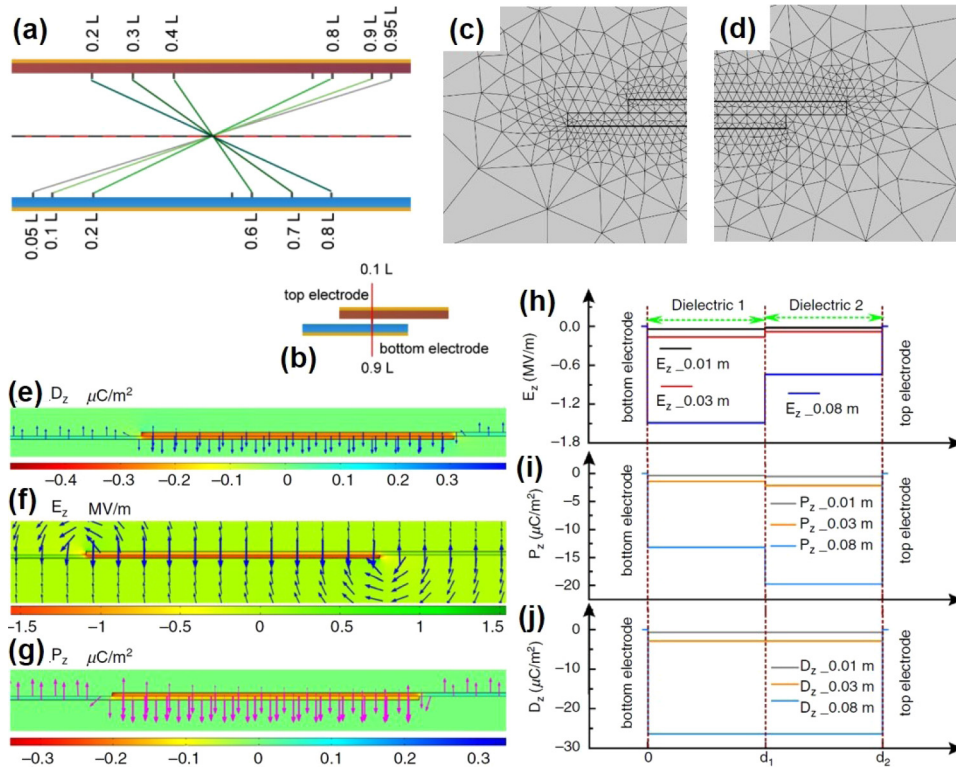


FIG. 18. Finite element modeling (FEM) simulation of the lateral-sliding mode TENG at open-circuit conditions, using the COMSOL multiphysics software. (a) Different positions in the top electrode–dielectric interface and bottom electrode–interface of the TENG; (b) cross-section of the TENG at the maximum separation distance of 0.9 L; finite element mesh for the material body (c) and free space (d) at the maximum separation distance; distribution of the z-component of (e) the electric displacement D_z , (f) the electric field E_z , and (g) the polarization vector P_z . E_z (h), P_z (i), and D_z (j) inside the dielectric for the overlapping area change with the relative movement of the two triboelectric surfaces.⁴⁶ Reproduced with permission from Shao *et al.*, *Appl. Phys. Rev.* **7**, 011405 (2020). Copyright 2020 AIP Publishing LLC.

V. ELECTROMECHANICAL COUPLING MODEL OF A TENG IN AN ENERGY HARVESTING SYSTEM

A. Triboelectric-electret nanogenerators (T-ENGs)

1. Governing equations of the T-ENGs

The triboelectric-based electret nanogenerator (T-ENG) represents one type of electrostatic kinetic energy harvesters (e-KEHs), based on a variable capacitive structure, and is generally made up of two/or more electrodes separated by a dielectric that is typically air (or vacuum) [Fig. 19(a)].⁷⁴ The dielectrics selected for a T-ENG are electret materials, i.e., polarized dielectric materials. Depending on the different electret fabrication processes, charges are injected on the surface or inside the dielectric layer. If an electret is created by contact electrification, it is called a triboelectret.^{75,76} Due to the distribution of charges on the triboelectret, an electric field is generated in the air and the triboelectret, respectively. The voltage at the surface of the triboelectret layer is derived by⁷⁴

$$V_{TE} \approx \sigma_{TE} d_{die} / \epsilon_{die} = Q_{TE} / C_{die}, \quad (94)$$

where σ_{TE} denotes the charge density in the triboelectret surface, Q_{TE} is the total surface charges; d_{die} , ϵ_{die} , and C_{die} represent the thickness, permittivity, and capacitance of the triboelectret, respectively. It is seen that V_{TE} depends on the triboelectric charges and the thickness of the triboelectric layer only but not

on the air gap if it is substantially larger than the thickness of the triboelectret. Similar to the TENG device, the T-ENG device is also governed by quasi-electrostatic laws. The equivalent electrical circuit model of this T-ENG device is demonstrated in Figs. 19(b) and 19(c). When an external load Z is connected between the two electrodes, according to Kirchhoff law and Ohm's law, the voltage across the Z is given by⁷⁴

$$Z \times \frac{dQ_{var}(t)}{dt} + \frac{Q_{var}(t)}{C_{T-ENG}(t)} = V_{TE}, \quad (95)$$

where Q_{var} represents the charges in the top electrode. C_{T-ENG} represents the capacitance of the T-ENG, which is

$$C_{T-ENG} = \frac{C_{var} C_{die}}{C_{var} + C_{die}} = S \frac{1}{\frac{d_{die}}{\epsilon_{die}} + \frac{d_{var}}{\epsilon_{air}}}, \quad (96)$$

where C_{var} is the capacitance of the air gap between the electret and the top electret; d_{var} and ϵ_{air} represent the air gap thickness and permittivity of the air, respectively. It should be noticed that Eq. (95) is a first-order differential equation with time-dependent coefficients, which cannot be solved analytically.⁷⁷ The solution of $Q_{var}(t)$ can be represented as an infinite Fourier series⁷⁸ which must be solved numerically using, e.g., SPICE or Simulink

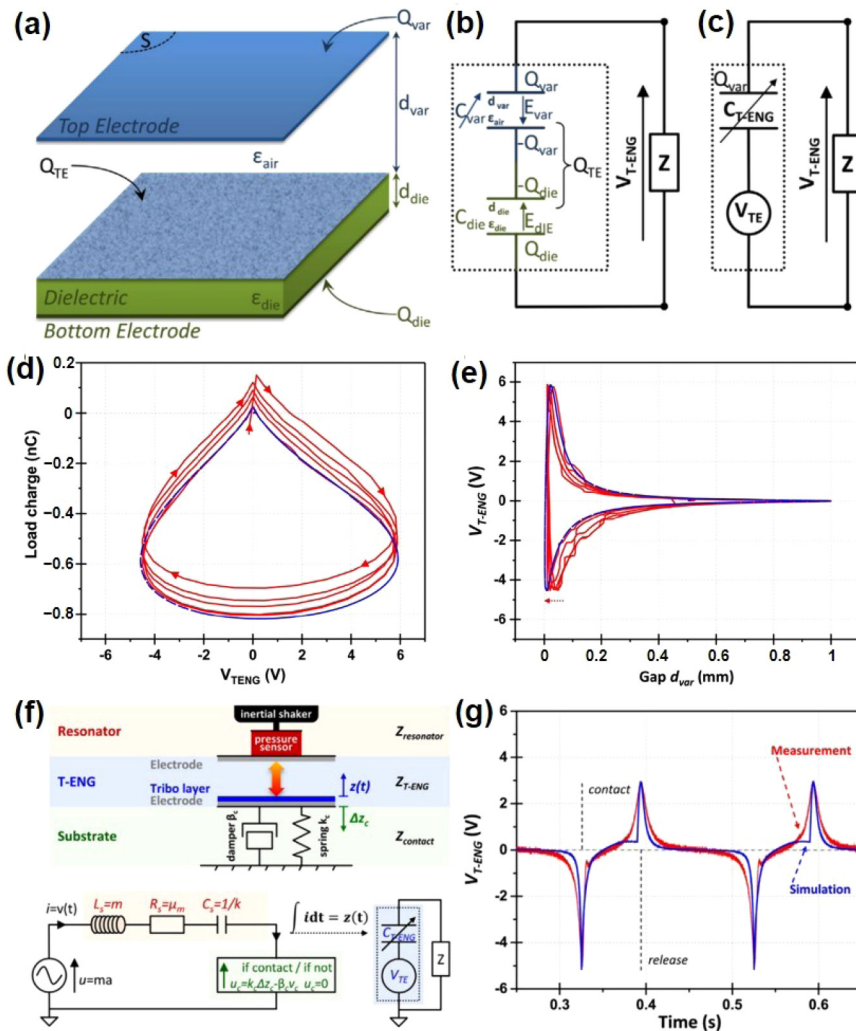


FIG. 19. Model of triboelectric-based electret nanogenerator (T-ENG) and its basic outputs. (a) Schematic illustration of the T-ENG in the vertical contact configuration, (b) equivalent circuit model of the T-ENG and parameters, and (c) compact electrical model of the T-ENG; (d) plots of charge–voltage, and (e) gap-voltage from the FEM simulation results; (f) the mechanical model of the T-ENG energy harvesting system including the resonator, triboelectric layer, and substrate; (g) comparison of the voltage through a load $Z_L = 10 \text{ M}\Omega$ between the experimental result and electrical modeling with a parasitic capacitance of 2.5 pF .⁷⁴ Reproduced with permission from Hinchet *et al.*, *Nano Energy* 47, 401 (2018). Copyright 2018 Elsevier.

software.^{41,74} From Eq. (96), it is found that the T-ENG structure is composed of two different capacitors. The first one is denoted C_{die} , which is a fixed-in-time capacitor depending on the thickness and permittivity of the triboelectret. The second one is C_{var} , which is a variable capacitor changing relation to the air gap distance between the top electrode and the triboelectret. Note that these two capacitors are connected in series.

The FEM simulations using COMSOL software are shown in Figs. 19(d) and 19(e). It is seen that the Q – V cycles [Fig. 19(d)] turn clockwise, meaning the energy is harvested. Thus, this T-ENG device is an energy generator. A voltage signal is generated at a very small gap, which is less than $200 \mu\text{m}$ from the triboelectret layer, and beyond this distance the generated signal is negligible. This is because the generated electrostatic force induced by electrostatic charges is reversely proportional to the square of the separation distance. In this way, it is demonstrated that the electrostatic energy harvesters are more efficient at microscale than at macroscale, a result that also applies to many other types of electrostatic energy harvesters either.

2. Lumped schematic model of the T-ENGs

The whole mechanical system of the T-ENG energy harvester is modeled including the inertial shaker, the T-ENG; a spring k and damping element c are utilized to represent the elastic contact between the top electrode and the triboelectric layer [Fig. 19(f)]. A comparison of experimental results and simulations for V_{T-ENG} [Fig. 19(g)] agrees well thus establishing the validity and practicality of this lumped-element model.

3. Similarities and differences between the TENGs and T-ENGs

The similarities and differences between the TENG and T-ENG can be summarized as

- (a) Basic structure: both of the two different energy harvesting devices consist of at least two electrodes and one dielectric layer. From this point, they are similar to each other.

- (b) Materials selection: for a TENG, materials that generate tribo-charges can be selected as tribo-pairs. However, only the so-called electret materials can be used for a T-ENG (such as the polypropylene, PTFE). Because the electrets are dielectric materials, T-ENGs constitute a sub-class of TENGs.
- (c) Models and working principles: the TENGs and T-ENGs share the same electric model: a constant voltage source, the value of which equals to the surface voltage of the triboelectret/ or triboelectric layer, in series with a variable capacitance of the TENG/or T-ENG. From the classical electrostatic theory, the T-ENG is also governed by the displacement current, and it belongs to the device category that employs Maxwell's displacement current as driving force for effective conversion of mechanical energy into electricity.

Consider the T-ENGs illustrated in Fig. 19(a) as an example: when the top electrode moves, output charges flow through the external circuit thereby reducing the potential difference. During operation, the charges distributed in the electrodes change as the separation distance changes, leading to a variation of total electric field within the T-ENG. As a result, a displacement current is generated. Additionally, it is known that the conduction current in the external circuit is equal to the displacement current in the internal circuit of T-ENGs under ideal conditions similar to the case with TENGs. In other words, the TENGs and T-ENGs share almost the same working principles.

B. Electromechanical coupling models of TENGs

In general, a TENG energy harvesting system requires a mechanical input (such as an external vibration) and an electrical input (the power management circuit, Fig. 2). The TENG device

couple the mechanical energy field and electrical energy field. So, an electromechanical coupling model is required to couple the mechanical equilibrium and electrical loop equations of the TENG energy harvesting system. The electromechanical coupling model usually contains a mechanical model and an equivalent electrical circuit model. The former and relevant dynamical equations are proposed to describe the mechanical dynamics of the system, which are strongly affected by the electrical operation of the TENG transducer.⁷⁹⁻⁸¹ The equivalent electrical circuit model of TENGs has been established based on the lumped parameter circuit theory.^{40,41} In general, the process of deriving the electromechanically coupled equations involves applying the Newton's second law for the moving part of a TENG device in the mechanical domain, Kirchhoff's loop law for the conditioning circuit.

Two different mechanical models for TENGs have been developed to simulate the harvester dynamics.⁷⁹⁻⁸¹ For a typical mechanical energy harvesting system in which a CS mode TENG is utilized as the energy transducer [Fig. 20(a)], its corresponding dynamical model is represented by a one-degree-of-freedom spring-mass-damper system [Figs. 20(b) and 20(c)]. Figures 20(b) and 20(c) illustrate schematically the system before and at the onset of impact, respectively, which means there are two scenarios for the motion of the movable part. For the second scenario, the system will be subject to a new spring force from the impact stiffness, k_i , except for the force due to the mechanical spring, k_{eq} . In other words, the stiffness and damping become piece-wise functions. Thus, two dynamic equations are needed to describe the motion. Therefore, the coupled governing equations of the coupled electromechanical system based on the piece-wise impact model and equivalent electrical circuit model can be written as⁷⁹

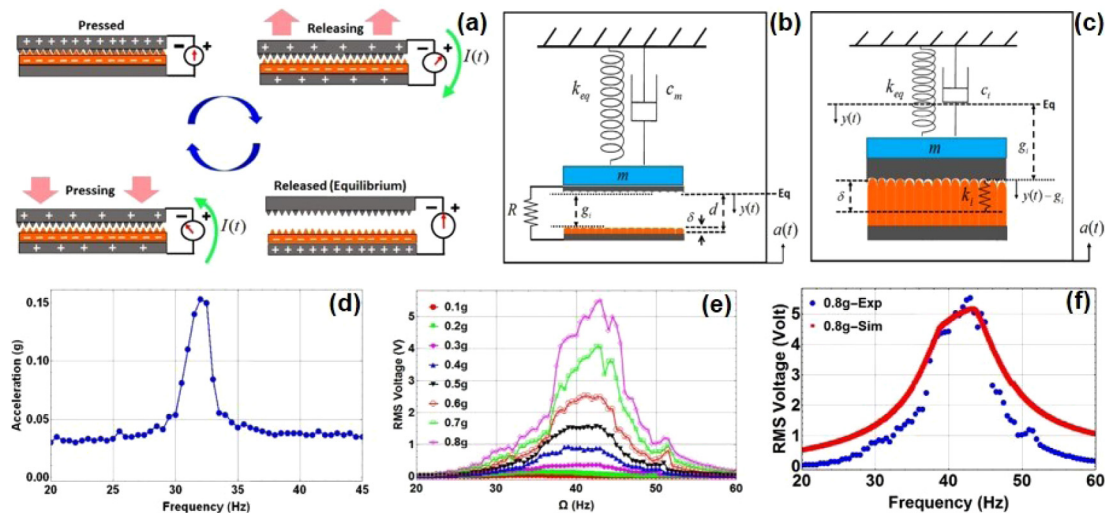


FIG. 20. Single-degree-of-freedom spring-mass-damper (SDOF) model of the vertical contact-separation mode TENG and the basic output performances. (a) Schematic illustration, (b) equivalent SDOF model before impact, (c) at the onset of impact (zoomed in); (d) the resonance frequency without impact at low excitation; (e) root-mean-square voltage of the TENG at different excitation levels with the resistance of $Z = 2 \text{ M}\Omega$; (f) comparison of root-mean-square voltage between the experimental and simulated results with estimated excitation level (0.8 g), surface charge densities, σ , and damping ratios, ζ .⁷⁹ Reproduced with permission from Ibrahim *et al.*, J. Sound Vib. **416**, 111 (2018). Copyright 2018 Elsevier.

$$m \frac{d^2 y}{dt^2} = -c_m \frac{dy}{dt} - k_{eq} y(t) + \frac{q^2(t)}{2\epsilon_r \epsilon_0 S} - ma, \quad y(t) < g_i, \quad (97.a)$$

$$m \frac{d^2 y}{dt^2} = -c_i \frac{dy}{dt} - k_{eq} y(t) - k_i y((t) - g_i) - ma, \quad y(t) \geq g_i, \quad (97.b)$$

$$\frac{dq}{dt} = -\frac{q(t)}{\epsilon_0 Z S} \left(\frac{T}{\epsilon_r} + d_0 - y(t) \right) + \frac{\sigma}{\epsilon_0 Z} (d_0 - y(t)). \quad (97.c)$$

Note that m represents the mass of the structure. c_i denotes the impact damping coefficient and k_i represents the impact stiffness coefficient. $y(t)$ is the relative displacement of the upper electrode with respect to the base measured from fixed initial reference, c_m represents the mechanical damping coefficient. k_{eq} is the equivalent stiffness for the clamped-clamped beam with the center mass, which is calculated by $k_{eq} = m(2\pi f_n)^2$, where f_n is the measured resonance frequency of the structure. F_e stands for the electrostatic force, and $a(t)$ represents the base excitation. It is apparent that the introduction of a piece-wise stiffness will yield a large frequency bandwidth of this system, and then enhance efficiency in energy conversion. As demonstrated in Fig. 20(e), the frequency bandwidths increases with excitation level to reach a maximum value of 10 Hz at 0.8 g excitation level. The bigger excitation amplitude will cause a large contact area and more generated charges, resulting in the increment of the tribocharge density [Fig. 20(f)].

For the contact freestanding mode TENG, a mechanical model based on the three-degree-of-freedom vibro-impact oscillator is proposed.^{80,81} Either the one-degree-of-freedom spring-mass-damper system or the three-degree-of-freedom vibro-impact oscillator system, these mechanical models mainly depend on the structural dynamic aspects and dynamic input that we are interested in. Moreover, the coupling effect enabling the two systems to be modeled as strongly coupled or weakly coupled should be considered and investigated simultaneously, which is mainly determined by the actual conditions.⁸²⁻⁹¹ It has been proved that the electrostatic force plays a key role in relation to the couplings and energy conversion.⁷⁴ Through this model, the optimal condition for an individual TENG to provide the maximum output power at a predetermined frequency can be obtained. For instance, when resonance oscillation takes place, the resonant TENGs can effectively harvest vibration energy due to the effect of impact stiffening.⁸² There is, however, still much work to obtain a detailed understanding.

VI. RELATIONSHIP AMONG VARIOUS MODELS

A. The lumped circuit abstraction and lumped matter discipline

The definition of lumped circuit abstraction is: “Capped a set of lumped elements that obey the lumped matter discipline (LMD) using ideal wires to form an assembly that performs a specific function results in the lumped circuit abstraction.”⁹²⁻⁹⁴ Here, the LMD always refers to a set of constraints that for the definitions or terminal interactions. If the LMD is adhered, the related circuit analysis and work with the lumped circuit abstraction can be simplified. The lumped matter discipline provides the foundation for the lumped circuit abstraction,

and is the fundamental mechanism by which the research is able to move from the field of physics to the field of electrical engineering.^{92,93}

When a circuit is adaptable with LMD, the circuit itself can be abstracted as a lumped element. The lumped element model of TENG is modeled by a voltage source in series with a variable capacitor. As an example, take the CS mode TENG shown in Fig. 6(c). Here, equal positive and negative charges are distributed on the tribo-surfaces and the two electrodes of TENGs. It is apparent that the TENG device is neutral at any time because of the law of charge conservation, i.e., the total charge within the TENG device is zero, and thus satisfies criterion for LMD. So, the TENG can be regarded as a lumped element.

B. Deriving Kirchhoff's law from Maxwell's equations

It has been shown that the TENG can be regarded as a lumped element. In general, the relevant Maxwell's equations and continuity equation,⁹²

$$\oint \mathbf{E} \cdot d\mathbf{l} = -\frac{\partial \phi_B}{\partial t}, \quad (98.a)$$

$$\oint \mathbf{J} \cdot d\mathbf{S} = -\frac{\partial q}{\partial t} \quad (98.b)$$

can be simplified to the following:

$$\oint \mathbf{E} \cdot d\mathbf{l} = 0, \quad (99.a)$$

$$\oint \mathbf{J} \cdot d\mathbf{S} = 0, \quad (99.b)$$

according to LMD or due to the constrained domain: $\partial \phi_B / \partial t = 0$, and $\partial q / \partial t = 0$. Equation (99.a) indicates that the line integral of the field around any closed path is zero. Applying Eq. (99.a) to the closed loop shown in Fig. 5(a), we get

$$\oint \mathbf{E} \cdot d\mathbf{l} = \int_A^B \mathbf{E} \cdot d\mathbf{l} + \int_B^A \mathbf{E} \cdot d\mathbf{l} = 0. \quad (100)$$

Because the potential difference V_{xy} across the xy terminal of an element is

$$V_{xy} = \int_x^y \mathbf{E} \cdot d\mathbf{l}. \quad (101)$$

Thus, we have (Fig. 5)

$$\begin{aligned} \oint \mathbf{E} \cdot d\mathbf{l} &= \int_A^B \mathbf{E} \cdot d\mathbf{l} + \int_B^A \mathbf{E} \cdot d\mathbf{l} = V_{AB} + V_{BA} = V_{AB} + IZ \\ &= V_{AB} + \frac{\partial Q}{\partial t} Z = 0, \end{aligned} \quad (102)$$

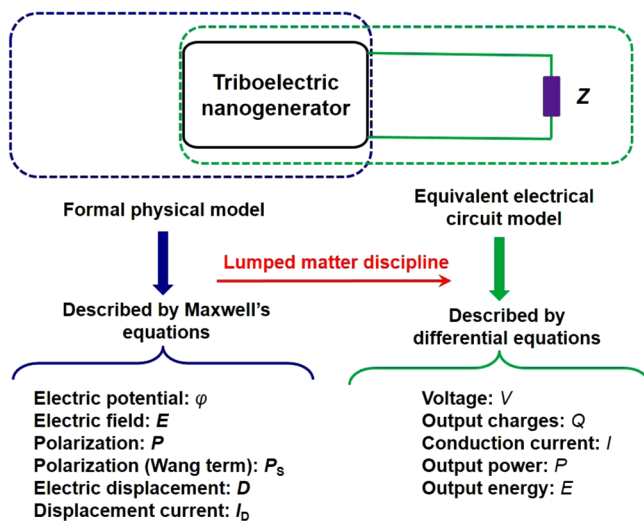


FIG. 21. Physical model and equivalent circuit model of TENGs built for different fields: the formal physical model is utilized to explore the physical variables within the TENGs while the equivalent electrical circuit model is developed to investigate the circuit variables in the external circuit. The equivalent electrical circuit model is essentially abstracted from the formal physical model due to the new abstraction layer created on top of Maxwell's Equations. The formal physical model is described by Maxwell's equations while the dynamic electric circuits can be analyzed through differential equations.

$$V_{AB} = \int_A^B \mathbf{E} \cdot d\mathbf{l} = -\frac{\partial Q}{\partial t} Z. \quad (103)$$

Equation (102) means that the algebraic sum of the voltages around any closed path in the circuit is equal to zero. In other words, combining the TENG model and LMD, the Kirchhoff's voltage law is derived from the Maxwell's equations. More importantly, it is apparent that the derived Eq. (103) is identical with Eq. (7). For these reasons, a map is sketched (Fig. 21) so as to express the relationship between the formal physical model and the equivalent electrical circuit model of TENGs. The formal physical model mainly refers to the quasi-electrostatic model, which is constructed from the Maxwell's equations. In particular, the methods of 3D mathematical modeling and DDEF modeling have been proposed to explore physical variables such as the electric potential (ϕ), electric field (E), polarization (Wang term, P_s) and so on. Similarly, the equivalent circuit models are developed from the lumped circuit abstraction, and the relevant dynamic electric circuits can be analyzed through differential equations owing to the LMD. In addition, the mechanical model is significantly affected by the electrical operation of the TENG device; for instance, it has been proved that the electrostatic force plays an important role with respect to the coupling coefficient in an electro-mechanical coupling model.

VII. SUMMARY

In conclusion, the goal of this review paper was to present a summary about TENG models developed as of today, which

included the formal physical model, equivalent electrical circuit model, mechanical model, and electromechanical coupling models of a TENG energy harvesting system. The main conclusions were drawn as follows:

- (1) A typical TENG energy harvesting system is composed by a resonator (mechanical excitation), a TENG transducer, and a power management circuit (conditioning circuit). Mechanical energy is first converted into electricity and stored in the TENG device as an electric field distribution. The electrical energy is then fed into the external circuit and extracted from there. The resonator works under mechanical triggering, while the power management circuit controls the extracted electrical energy; the TENG harvester couples the mechanical and electrical energy fields.
- (2) Based on the Maxwell's equations, the quasi-electrostatic model is established, which essentially belongs to the formal physical model of TENGs, and can be numerically described by the methods of three-dimensional mathematical modeling and distance-dependent electric field modeling. These models allow us to determine the change of physical variables such as the electric potential ϕ , electric field E , electric displacement D , polarization P , polarization (Wang term) P_s , displacement current I_D , from which the fundamentals of TENGs can be clearly explored.
- (3) The equivalent electrical circuit models of TENGs include the conventional capacitive model and Norton's equivalent circuit model, which are proposed according to the lumped parameter circuit theory. The TENG device is neutral at any time and thus can be regarded as a lumped element. In effect, the TENG is represented by a voltage source in series with a variable capacitor; yet it can also be regarded as a combination of a time-variant source and the TENG internal impedance according to the Norton's equivalent circuit model.
- (4) The mechanical model and relevant dynamic equations describe the structural dynamic behaviors of the TENG energy harvesting system. These configurations can be represented by a one degree-of-freedom spring-mass-damper system or a three-degree-of-freedom vibro-impact oscillator system, depending on the actual conditions. Combining the electrical sub-models, an electromechanical coupling model for the TENG energy harvesting system is constructed, through which the dynamic input conditions, electrical output conditions, as well as the coupling effects can be explored. Finally, the optimum conditions and maximum energy harvesting output as well as the related total energy conversion efficiency can be modeled and predicted.
- (5) Because the TENG device satisfies LMD, Kirchhoff's law and the governing equations of TENGs can be derived from the Maxwell's equations. The formal physical models of TENGs are described by Maxwell's equations in the physical field while the equivalent electrical circuit models of TENGs are dominated by the lumped circuit abstraction theory. By use of LMD, one can easily move from the field of physics to the field of electrical engineering.

Fundamental sciences and advanced technological applications are closely coupled in the context of TENG devices. Models of TENGs

provide a powerful and strong bridge to connect core science problems and engineering applications together, from which more and more quantitative research and evaluation can be carried out. We emphasize that we did not consider generation of tribo-charges, edge effects, air breakdown, etc. in this review.^{95–101} It is, however, our hope that this review can provide a guide for understanding the basic models and fundamentals of TENGs toward more sophisticated applications in the near future.

ACKNOWLEDGMENTS

Research was supported by the National Key R&D Project from Minister of Science and Technology (Grant No. 2016YFA0202704), National Natural Science Foundation of China (Grant Nos. 51432005 and 51702018), and China Postdoctoral Science Foundation (Grant No. 2019M660766).

DATA AVAILABILITY

The data that support the findings of this study are available from the corresponding author upon reasonable request.

REFERENCES

- ¹Z. L. Wang, *Mater. Today* **20**, 74 (2017).
- ²Z. L. Wang, *Nano Energy* **68**, 104272 (2020).
- ³R. Hinchet, H. J. Yoon, H. Ryu, M. K. Kim, E. K. Choi, D. S. Kim, and S. W. Kim, *Science* **365**, 491 (2019).
- ⁴J. J. Shao, M. Willatzen, J. Y. Shi, and Z. L. Wang, *Nano Energy* **60**, 630 (2019).
- ⁵A. Y. Li, Y. Zi, H. Guo, Z. L. Wang, and F. M. Fernandez, *Nat. Nanotechnol.* **12**, 481 (2017).
- ⁶Z. L. Wang, *Adv. Energy Mater.* **10**, 2000137 (2020).
- ⁷Z. L. Wang and A. C. Wang, *Mater. Today* **30**, 34 (2019).
- ⁸S. Boisseau, G. Despesse and B. A. Seddik, *Electrostatic Conversion for Vibration Energy Harvesting* (Small-Scale Energy Harvesting, Intech Open Ltd, London, UK, 2012).
- ⁹D. Briand, E. Yeatman, and S. Roundy, *Micro Energy Harvesting* (Wiley-ISTE, 2015).
- ¹⁰P. Basset, E. Blokhina, and D. Galayko, *Electrostatic Kinetic Energy Harvesting* (Wiley-ISTE, 2016).
- ¹¹S. P. Beeby and T. O'Donnell, *Energy Harvesting Technologies* (Springer, NY, 2009).
- ¹²F. R. Fan, Z. Q. Tian, and Z. L. Wang, *Nano Energy* **1**, 328 (2012).
- ¹³J. Chen, Y. Huang, N. Zhang, H. Zou, R. Liu, C. Tao, X. Fan, and Z. L. Wang, *Nat. Energy* **1**, 16138 (2016).
- ¹⁴W. Kim, D. Bhatia, S. Jeong, and D. Choi, *Nano Energy* **56**, 307 (2019).
- ¹⁵M. Willatzen and Z. L. Wang, *Nano Energy* **61**, 311 (2019).
- ¹⁶H. T. Baytekin, A. Z. Patashinski, M. Branicki, B. Baytekin, S. Soh, and B. A. Grzybowski, *Science* **333**, 308 (2011).
- ¹⁷M. Willatzen and Z. L. Wang, *Nano Energy* **52**, 517 (2018).
- ¹⁸A. Erturk and D. J. Inman, *J. Intel. Mater. Syst. Struct.* **19**, 1311 (2008).
- ¹⁹Z. Yang, A. Erturk, and J. Zu, *Extreme. Mech. Lett.* **15**, 26 (2017).
- ²⁰K. Ikezaki, M. Miki, and J. Tamura, *Jpn. J. Appl. Phys.* **20**, 1741 (1981).
- ²¹L. S. McCarty, A. Winkleman, and G. M. Whitesides, *J. Am. Chem. Soc.* **129**, 4075 (2007).
- ²²Y. Lu, M. C. Chichi, Y. L. Wang, and P. Basset, *Smart Mater. Struct.* **27**, 014001 (2017).
- ²³B. Gross and R. J. de Moraes, *J. Chem. Phys.* **37**, 710 (1962).
- ²⁴Z. L. Wang, L. Lin, J. Chen, S. M. Niu, and Y. L. Zi, *Triboelectric Nanogenerators* (Springer, Switzerland, 2016).
- ²⁵Y. Zhang, Y. Fang, J. Li, Q. Zhou, Y. Xiao, K. Zhang, B. Luo, J. Zhou, and B. Hu, *ACS Appl. Mater. Interfaces* **9**, 37493 (2017).
- ²⁶K. Tian, J. Bae, S. E. Bakarich, C. Yang, R. D. Gately, G. M. Spinks, M. I. H. Panhuis, Z. Suo, and J. J. Vlassak, *Adv. Mater.* **29**, 1604827 (2017).
- ²⁷G. Q. Xu, X. Y. Li, X. Xia, J. J. Fu, W. B. Ding, and Y. L. Zi, *Nano Energy* **59**, 154 (2019).
- ²⁸S. H. Shin, Y. H. Kwon, Y. H. Kim, J. Y. Jung, and J. Nah, *Nanomaterials* **6**, 10 (2016).
- ²⁹Q. Shi, H. Wu, H. Wang, H. Wu, and C. Lee, *Adv. Eng. Mater.* **7**, 1701300 (2017).
- ³⁰Q. Shen, X. Xie, M. Peng, N. Sun, H. Shao, H. Zheng, Z. Wen, and X. Sun, *Adv. Funct. Mater.* **28**, 1703420 (2018).
- ³¹C. R. S. Rodrigues, C. A. S. Alves, J. Puga, A. M. Pereira, and J. O. Ventura, *Nano Energy* **30**, 379 (2016).
- ³²Y. Zi, S. Niu, J. Wang, Z. Wen, W. Tang, and Z. L. Wang, *Nat. Commun.* **6**, 8376 (2015).
- ³³J. Qian, D. S. Kim, and D. W. Lee, *Nano Energy* **49**, 126 (2018).
- ³⁴J. Park, A. Y. Choi, C. J. Lee, D. Kim, and Y. T. Kim, *RSC Adv.* **7**, 54829 (2017).
- ³⁵J. P. Lee, B. U. Ye, K. N. Kim, J. W. Lee, W. J. Choi, and J. M. Baik, *Nano Energy* **38**, 377 (2017).
- ³⁶D. Kim, I. W. Tcho, and Y. K. Choi, *Nano Energy* **52**, 256 (2018).
- ³⁷S. A. Khan, H. L. Zhang, Y. Xie, M. Gao, M. A. Shah, A. Qadir, and Y. Lin, *Adv. Eng. Mater.* **19**, 1600710 (2017).
- ³⁸Q. Jing, Y. S. Choi, M. Smith, N. Catic, C. Ou, and S. K. Narayan, *Adv. Mater. Technol.* **4**, 1800328 (2019).
- ³⁹H. Askari, Z. Saadatnia, A. Khajepour, M. B. Khamesee, and J. Zu, *Adv. Eng. Mater.* **19**, 12 (2017).
- ⁴⁰S. M. Niu and Z. L. Wang, *Nano Energy* **14**, 161 (2015).
- ⁴¹S. M. Niu, Y. S. Zhou, S. Wang, Y. Liu, L. Lin, Y. Bando, and Z. L. Wang, *Nano Energy* **8**, 150 (2014).
- ⁴²Z. L. Wang, T. Jiang, and L. Xu, *Nano Energy* **39**, 9 (2017).
- ⁴³K. Dai, X. Wang, S. Niu, F. Yi, Y. Yin, L. Chen, Y. Zhang, and Z. You, *Nano Res.* **10**, 157 (2017).
- ⁴⁴J. J. Shao, T. Jiang, and Z. L. Wang, *Sci. China. Technol. Sci.* **63**, 1087 (2020).
- ⁴⁵J. J. Shao, M. Willatzen, T. Jiang, W. Tang, X. Chen, J. Wang, and Z. L. Wang, *Nano Energy* **59**, 380 (2019).
- ⁴⁶J. J. Shao, D. Liu, M. Willatzen, and Z. L. Wang, *Appl. Phys. Rev.* **7**, 011405 (2020).
- ⁴⁷R. D. I. G. Dharmasena, K. D. G. I. Jayawardena, C. A. Mills, J. H. B. Deane, J. V. Anguita, R. A. Dorey, and S. R. P. Silva, *Energy Environ. Sci.* **10**, 1801 (2017).
- ⁴⁸R. D. I. G. Dharmasena, K. D. G. I. Jayawardena, C. A. Mills, R. A. Dorey, and S. R. P. Silva, *Nano Energy* **48**, 391 (2018).
- ⁴⁹M. Lu, W. Yin, A. Peyton, Z. Qu, X. Meng, Y. Xie, P. Zhao, J. Luo, Q. Zhao, Y. Tao, T. Zhou, and Z. Zhang, *Nano Energy* **63**, 103883 (2019).
- ⁵⁰S. M. Niu, Y. Liu, S. H. Wang, L. Lin, Y. S. Zhou, Y. F. Hu, and Z. L. Wang, *Adv. Funct. Mater.* **24**, 3332 (2014).
- ⁵¹S. M. Niu, Y. Liu, S. Wang, L. Lin, Y. S. Zhou, Y. Hu, and Z. L. Wang, *Adv. Mater.* **25**, 6184 (2013).
- ⁵²R. D. I. G. Dharmasena and S. R. P. Silva, *Nano Energy* **62**, 530 (2019).
- ⁵³S. M. Niu, Y. Liu, X. Chen, S. Wang, Y. S. Zhou, L. Lin, Y. Xie, and Z. L. Wang, *Nano Energy* **12**, 760 (2015).
- ⁵⁴S. M. Niu, S. H. Wang, L. Lin, Y. Liu, Y. S. Zhou, Y. F. Hu, and Z. L. Wang, *Energy Environ. Sci.* **6**, 3576 (2013).
- ⁵⁵J. J. Shao, T. Jiang, W. Tang, X. Chen, L. Xu, and Z. L. Wang, *Nano Energy* **51**, 688 (2018).
- ⁵⁶J. J. Shao, W. Tang, T. Jiang, X. Y. Chen, L. Xu, B. D. Chen, T. Zhou, C. R. Deng, and Z. L. Wang, *Nanoscale* **9**, 9668 (2017).
- ⁵⁷J. J. Shao, T. Jiang, W. Tang, L. Xu, T. W. Kim, C. Wu, X. Chen, B. Chen, T. Xiao, Y. Bai, and Z. L. Wang, *Nano Energy* **48**, 292 (2018).
- ⁵⁸J. Peng, S. D. Kang, and G. J. Snyder, *Sci. Adv.* **3**, eaap8576 (2017).
- ⁵⁹H. Zhang, S. Feng, D. He, P. Molinié, and J. Bai, *Nano Energy* **63**, 103856 (2019).
- ⁶⁰R. D. I. G. Dharmasena, J. H. B. Deane, and S. R. P. Silva, *Adv. Energy Mat.* **8**, 1802190 (2018).

- ⁶¹J. H. B. Deane, R. D. I. G. Dharmasena, and G. Gentile, *Nano Energy* **54**, 39 (2018).
- ⁶²H. Zhang, L. Quan, J. Chen, C. Xu, C. Zhang, S. Dong, C. Lü, and J. Luo, *Nano Energy* **56**, 700 (2019).
- ⁶³H. Zhang, C. Zhang, J. Zhang, L. Quan, H. Huang, J. Jiang, S. Dong, and J. Luo, *Nano Energy* **61**, 442 (2019).
- ⁶⁴R. W. Pryor, Multiphysics modeling: Using COMSOL 5 and MATLAB, 2016, see 1938549988.
- ⁶⁵P. Vasandani, Z. H. Mao, W. Jia, and M. Sun, *Simul. Model. Pract. Theory* **68**, 95 (2016).
- ⁶⁶G. S. Maximous, A. M. Fatahalla, A. Seley, T. A. Ali, H. Mostafa, and IEEE, in *2018 16th IEEE International New Circuits and Systems Conference* (IEEE, NY, 2018), p. 331.
- ⁶⁷Y. Zhu, B. Yang, J. Liu, X. Wang, L. Wang, X. Chen, and C. Yang, *Sci. Rep.* **6**, 22233 (2016).
- ⁶⁸P. Vasandani, Z. H. Mao, W. Jia, and M. Sun, *J. Electrostat.* **90**, 147 (2017).
- ⁶⁹B. D. Chen, W. Tang, C. He, C. R. Deng, L. J. Yang, L. P. Zhu, J. Chen, J. J. Shao, L. Liu, and Z. L. Wang, *Mater. Today* **21**, 88 (2018).
- ⁷⁰T. X. Xiao, X. Liang, T. Jiang, L. Xu, J. J. Shao, J. H. Nie, Y. Bai, W. Zhong, and Z. L. Wang, *Adv. Funct. Mater.* **28**, 1802634 (2018).
- ⁷¹A. Zaky, A. Ahmed, P. Ibrahim, B. Mahmoud, and H. Mostafa, paper presented at the 2018 IEEE 61st International Midwest Symposium on Circuits and Systems (MWSCAS), 2018.
- ⁷²R. W. Pryor, Multiphysics Modeling Using COMSOL: A First Principles Approach, 2009.
- ⁷³C. Zhang, L. Liu, L. Zhou, X. Yin, X. Wei, Y. Hu, Y. Liu, S. Chen, J. Wang, and Z. L. Wang, *ACS Nano* **14**, 7092 (2020).
- ⁷⁴R. Hinchet, A. Ghaffarinejad, Y. Lu, J. Y. Hasani, S. W. Kim, and P. Basset, *Nano Energy* **47**, 401 (2018).
- ⁷⁵M. Eguchi, *Philos. Mag. Ser.* **6**, 178 (1925).
- ⁷⁶O. D. Jefimenko and D. K. Walker, *IEEE Trans. Ind. Appl.* **14**, 537 (1978).
- ⁷⁷E. Blokhina, D. Galayko, P. Basset, and O. Feely, *IEEE Trans. Circuits Syst. I Regul. Pap.* **60**, 875 (2013).
- ⁷⁸D. Galayko and P. Basset, *IEEE Trans. Circuits Syst. I Regul. Pap.* **58**, 299 (2011).
- ⁷⁹A. Ibrahim, A. Ramini, and S. Towfighian, *J. Sound Vib.* **416**, 111 (2018).
- ⁸⁰Y. Fu, H. Ouyang, and R. B. Davis, *Mech. Syst. Signal Process.* **121**, 509 (2019).
- ⁸¹Y. Fu, H. Ouyang, and R. B. Davis, *Nonlinear Dynam.* **92**, 1985 (2018).
- ⁸²D. Bhatia, W. Kim, S. Lee, S. W. Kim, and D. Choi, *Nano Energy* **33**, 515 (2017).
- ⁸³P. Basset, D. Galayko, A. M. Paracha, F. Marty, A. Dudka, and T. Bourouina, *J. Micromech. Microeng.* **19**, 115025 (2009).
- ⁸⁴H. Liu, C. Lee, T. Kobayashi, C. J. Tay, and C. Quan, *Smart Mater. Struct.* **21**, 035005 (2012).
- ⁸⁵B. N. J. Persson, *J. Chem. Phys.* **115**, 3840 (2001).
- ⁸⁶M. L. Seol, S. H. Lee, J. W. Han, D. Kim, G. H. Cho, and Y. K. Choi, *Nano Energy* **17**, 63 (2015).
- ⁸⁷D. Liu, B. Chen, J. An, C. Li, G. Liu, J. Shao, W. Tang, C. Zhang, and Z. L. Wang, *Nano Energy* **73**, 104819 (2020).
- ⁸⁸W. Yang, X. Wang, H. Li, J. Wu, and Y. Hu, *Nano Energy* **51**, 241 (2018).
- ⁸⁹W. Yang, X. Wang, H. Li, J. Wu, Y. Hu, Z. Li, and H. Liu, *Nano Energy* **57**, 41 (2019).
- ⁹⁰C. Jin, D. S. Kia, M. Jones, and S. Towfighian, *Nano Energy* **27**, 68 (2016).
- ⁹¹W. Zhang, D. Diao, K. Sun, X. Fan, and P. Wang, *Nano Energy* **48**, 456 (2018).
- ⁹²A. Anant, L. Jeffrey, *Foundations of Analog & Digital Electronic Circuits*, 1st ed. (Morgan Kaufmann, MA, 2005).
- ⁹³Computation Structures, M.I.T. Department of Electrical Engineering and Computer Science, see <https://computationstructures.org/>.
- ⁹⁴C. K. Alexander and M. N. O. Sadiku, *Fundamentals of Electric Circuits* (McGraw-Hill Education, 2017).
- ⁹⁵H. Zou, Y. Zhang, L. Guo, P. Wang, X. He, G. Dai, H. Zheng, C. Chen, A. C. Wang, C. Xu, and Z. L. Wang, *Nat. Commun.* **10**, 1427 (2019).
- ⁹⁶S. Matsusaka, H. Maruyama, T. Matsuyama, and M. Ghadiri, *Chem. Eng. Sci.* **65**, 5781 (2010).
- ⁹⁷R. R. Gokul and C. V. Krishnamurthy, *J. Electrostat.* **87**, 19 (2017).
- ⁹⁸K. Sayfidinov, S. D. Cezan, B. Baytekin, and H. T. Baytekin, *Sci. Adv.* **4**, eaau3808 (2018).
- ⁹⁹Q. Li, A. Peer, I. H. Cho, R. Biswas, and J. Kim, *Nat. Commun.* **9**, 974 (2018).
- ¹⁰⁰S. Wang, Y. Xie, S. Niu, L. Lin, C. Liu, Y. S. Zhou, and Z. L. Wang, *Adv. Mater.* **26**, 6720 (2014).
- ¹⁰¹Y. L. Zi, C. Wu, W. Ding, and Z. L. Wang, *Adv. Funct. Mater.* **27**, 1700049 (2017).